The Astrophysical Journal Supplement Series, 143:469–497, 2002 December
© 2002. The American Astronomical Society. All rights reserved. Printed in U.S.A.

THE PHYSICAL CONDITIONS FOR MASSIVE STAR FORMATION: DUST CONTINUUM MAPS AND MODELING

Kaisa E. Mueller, Yancy L. Shirley, Neal J. Evans II, and Heather R. Jacobson
Department of Astronomy, University of Texas at Austin, Austin, TX 78712-1083; mueller@astro.as.utexas.edu, yshirley@astro.as.utexas.edu, nje@astro.as.utexas.edu, hrj@astro.as.utexas.edu
Received 2002 June 25; accepted 2002 July 15

ABSTRACT

Fifty-one dense cores associated with water masers were mapped at 350 μm. These cores are very luminous, $10^3 < L_{\rm bol}/L_\odot < 10^6$, indicative of the formation of massive stars. Dust continuum contour maps, radial intensity profiles, and photometry are presented for these sources. The submillimeter dust emission peak is, on average, nearly coincident with the water maser position. The spectral energy distributions and normalized radial profiles of dust continuum emission were modeled for 31 sources using a one-dimensional dust radiative transfer code, assuming a power-law density distribution in the envelope, $n = n_f (r/r_f)^{-p}$. The best-fit density power-law exponent, p, ranged from 0.75 to 2.5 with $\langle p \rangle = 1.8 \pm 0.4$, similar to the mean value found recently by Beuther and coworkers in a large sample of massive star-forming regions. The mean value of p is also comparable to that found in regions forming only low-mass stars, but $\langle n_f \rangle$ is over 2 orders of magnitude greater for the massive cores. The mean p is incompatible with a logatropic sphere ($p = 1$), but other star formation models cannot be ruled out. Different mass estimates are compared and mean masses of gas and dust are reported within a half-power radius determined from the dust emission, $\langle \log M(< r_{\rm dec}) \rangle = 2.0 \pm 0.6$, and within a radius where the total density exceeds 10^4 cm^{-3}, $\langle \log M(< r_n) \rangle = 2.5 \pm 0.6$. Evolutionary indicators commonly used for low-mass star formation, such as $T_{\rm bol}$ and $L_{\rm bol}/L_{\rm smm}$, may have some utility for regions forming massive stars. Additionally, for comparison with extragalactic star formation studies, the luminosity–to–dust mass ratio is calculated for these sources, $\langle L_{\rm bol}/M_D \rangle = 1.4 \times 10^4\ L_\odot/M_\odot$, with a method most parallel to that used in studies of distant galaxies. This ratio is similar to that seen in high-redshift starburst galaxies.

Subject headings: dust, extinction — stars: early-type — stars: formation — submillimeter

On-line material: machine-readable tables

1. INTRODUCTION

The study of regions forming massive stars is essential to our understanding of how stars are born. Since most stars form in clusters associated with high-mass stars (e.g., Carpenter 2000), many recent studies have focused on better understanding the physical conditions in these regions (e.g., van der Tak et al. 2000; Sridharan et al. 2002; Beuther et al. 2002; Hatchell et al. 2000; Walsh et al. 2001; Osorio, Lizano, & D'Alessio 1999; Garay & Lizano 1999). The density distribution in the envelopes of regions forming massive stars is an important observational constraint for star formation models. The density distribution is usually a power law ($n \propto r^{-p}$). For example, McLaughlin & Pudriz's (1997) logatropic sphere model predicts a shallow power law with $p = 1$ in the static envelope, whereas Shu's (1977) inside-out collapse model for isolated star formation has an initial density distribution with $p = 2$.

A power-law density distribution has been fitted to observations of low-mass star-forming regions. Shirley, Evans, & Rawlings (2002b) and Young et al. (2003) find a combined $\langle p \rangle = 1.6 \pm 0.4$ for Class 0 (André, Ward-Thompson, & Barsony 1993) and Class I sources (Lada & Wilking 1984; Lada 1987; Myers & Ladd 1993; Chen et al. 1995). All "errors" on mean values in this paper refer to the standard deviation of the distribution of values about the mean. Shirley et al. (2002b) and Young et al. (2003) also report that aspherical cores have shallower power laws. If the aspherical cores are left out of the average for the low-mass cores, $\langle p \rangle$ goes to 1.8. While low-mass cores are well studied, it is only recently that the density structure of high-mass cores has been investigated for large samples. For example, van der Tak et al. (2000) found a shallow density structure, $\langle p \rangle = 1$–1.5, for a sample of 14 regions forming massive stars, while Beuther et al. (2002) reported $\langle p \rangle = 1.6 \pm 0.5$ for a larger sample of 69 massive star-forming regions.

Studies of massive star-forming cores also have important implications for understanding extragalactic star formation, including starburst galaxies. The far-infrared (FIR) luminosity–to–dust mass ratio, L/M, is a tool often used in extragalactic studies to characterize star formation since it is proportional to the star formation rate per unit mass (Kennicutt 1998). To learn if starburst galaxies are forming stars by mechanisms similar to those in the Milky Way, but on grander scales, it is important to investigate the star formation efficiency and L/M for dense gas in more accessible Galactic star formation regions to provide a point of comparison between these modes of star formation.

1.1. *The Sample*

The objects in this study were selected from the sample of Plume, Jaffe, & Evans (1992) and Plume et al. (1997) of massive star-forming cores associated with water masers. Table 1 lists the sources and their observed properties. Water masers are associated with regions of very dense gas ($n \geq 10^{10}$ cm^{-3}; Elitzur, Hollenbach, & McKee 1989). Each of the cores had been mapped in the CS $J = 5 \rightarrow 4$ transition (Shirley et al. 2002a) and detected in the CS $J = 7 \rightarrow 6$

TABLE 1

OBSERVED PROPERTIES

Source	α (1950.0)	δ (1950.0)	D (kpc)	Centroid[a] (arcsec)	350 μm S_ν[b] (Jy)	θ_{ap} (arcsec)	D Reference
IRAS 00338+6312	00 33 53.3	63 12 31	0.85	(−10, −5)	160 ± 32	30	1
					410 ± 82	120	
G123.07−6.31	00 49 29.2	56 17 36	2.2	(−15, −9)	160 ± 32	30	2
					290 ± 58	120	
W3[c,d]	02 21 53.1	61 52 20	2.3	(−30, 9)	30 ± 6	30	3
					220 ± 44	120	
W3(OH)	02 23 17.3	61 38 58	2.4	(7, −2)	400 ± 80	30	2
					1130 ± 230	120	
IRAS 02395+6244	02 39 31.0	62 44 16	8.1	(−9, 12)	20 ± 4	30	4
IRAS 02461+6147	02 46 11.7	61 47 34	4.5	(−9, 4)	20 ± 4	30	4
G137.07−3.00	02 54 11.2	56 17 36	4.9	(1, 10)	20 ± 4	30	2
GL 490[c]	03 23 38.9	58 36 33	0.9	(−3, 2)	80 ± 16	30	5
					180 ± 36	120	
Ori-IRc2	05 32 47.0	−05 24 24	0.45	(−4, 3)	1940 ± 390	30	4
					7680 ± 1540	120	
S231	05 35 51.3	35 44 16	2.3	(0, 0)	190 ± 38	30	2
					522 ± 100	120	
S235[d]	05 37 31.8	35 40 18	1.6	(1, 11)	50 ± 10	30	2
					240 ± 48	120	
S241	06 00 40.9	30 14 54	4.7	(8, 9)	30 ± 6	30	2
					40 ± 8	120	
Mon R2[d]	06 05 17.0	−06 22 40	0.9	(15, 10)	150 ± 30	30	2
					1400 ± 280	120	
S252A	06 05 36.5	20 39 34	1.5	(2, 6)	130 ± 26	30	2
					320 ± 64	120	
RCW 142	17 47 04.0	−28 53 42	2.0	(−5, 8)	530 ± 110	30	2
					670 ± 130	120	
W28A2[c]	17 57 26.8	−24 03 54	2.6	(0, −3)	950 ± 190	30	2
					1580 ± 320	120	
M8E	18 01 49.1	−24 26 57	1.8	(−8, 3)	210 ± 42	30	2
					380 ± 76	120	
G9.62+0.10	18 03 16.0	−20 32 01	5.7	(0, 3)	590 ± 120	30	6
					1150 ± 230	120	
G8.67−0.36	18 03 18.6	−21 37 59	4.5	(1, 4)	650 ± 130	30	7
					1160 ± 230	120	
G10.60−0.40	18 07 30.7	−19 56 28	6.5	(0, −1)	1110 ± 220	30	2
					1900 ± 380	120	
G12.42+0.50	18 07 56.4	−17 56 37	2.1	(−10, 0)	210 ± 42	30	8
					440 ± 88	120	
G12.89+0.49	18 08 56.3	−17 32 16	3.5	(0, 0)	220 ± 44	30	7
					340 ± 68	120	
G12.21−0.10	18 09 43.7	−18 25 09	13.7	(−5, 5)	230 ± 46	30	9
G13.87+0.28	18 11 41.5	−16 46 34	4.4	(10, −8)	190 ± 38	30	10
					430 ± 86	120	
W33A[c]	18 11 44.0	−17 53 09	4.0	(3, 4)	350 ± 70	30	4
					960 ± 190	120	
G14.33−0.64	18 16 00.8	−16 49 06	2.6	(0, −4)	440 ± 88	30	7
					830 ± 170	120	
GL 2136[c]	18 19 36.6	−13 31 40	2.0	(8, −9)	240 ± 48	30	11
					520 ± 100	120	
G19.61−0.23	18 24 50.1	−11 58 22	4.0	(2, −6)	460 ± 92	30	2
					500 ± 200	120	
G23.95+0.16[d]	18 31 40.8	−07 57 17	5.8	(7, 0)	100 ± 20	30	2
					320 ± 64	120	
G24.49−0.04	18 33 22.8	−07 33 54	3.5	(7, 3)	190 ± 37	30	2
					190 ± 37	120	
W43S	18 43 26.7	−02 42 40	8.5	(2, 4)	360 ± 72	30	2
					440 ± 88	120	
G31.41+0.31	18 44 59.5	−01 16 07	7.9	(−1, 0)	460 ± 92	30	10
					740 ± 150	120	
G40.50+2.54	18 53 45.6	07 49 16	2.1	(2, 1)	240 ± 48	30	8
					600 ± 120	120	
G35.58−0.03	18 53 51.4	02 16 29	3.5	(2, −3)	110 ± 22	30	2

TABLE 1—*Continued*

Source	α (1950.0)	δ (1950.0)	D (kpc)	Centroid[a] (arcsec)	350 μm S_ν[b] (Jy)	θ_{ap} (arcsec)	D Reference
					120 ± 24	120	
G45.07+0.13	19 11 00.3	10 45 42	9.7	(−2, −2)	180 ± 36	30	2
G48.61+0.02	19 18 13.1	13 49 44	11.8	(0, −2)	100 ± 20	30	2
					200 ± 40	120	
W51M[d]	19 21 26.2	14 24 36	7.0	(−29, −18)	280 ± 56	30	3
					3690 ± 740	120	
S87[d]	19 44 14.0	24 28 10	2.3	(0, −3)	140 ± 28	30	2
					310 ± 62	120	
S88B	19 44 42.0	25 05 30	2.0	(20, −10)	150 ± 30	30	2
					540 ± 110	120	
ON 1	20 08 09.9	31 22 42	6.0	(0, −10)	320 ± 64	30	2
					650 ± 130	120	
ON 2S	20 19 48.9	37 15 52	5.5	(5, −2)	200 ± 40	30	2
					510 ± 100	120	
S106[d]	20 25 32.8	37 12 54	4.1	(0, −5)	110 ± 22	30	3
					400 ± 80	120	
GL 2591[c]	20 27 35.5	40 01 13	1.0	(6, −2)	230 ± 46	30	12
					440 ± 88	120	
G97.53+3.19	21 30 37.0	55 40 36	8.5	(0, −12)	50 ± 10	30	4
					90 ± 18	120	
BFS 11-B	21 41 57.6	65 53 17	2.0	(1, −1)	40 ± 8	30	2
					90 ± 18	120	
S140[c]	22 17 41.1	63 03 42	0.90	(−10, −4)	350 ± 70	30	8
					1210 ± 240	120	
CEP A	22 54 19.2	61 45 44	0.73	(−1, −5)	430 ± 86	30	5
					1500 ± 300	120	
S158	23 11 36.1	61 10 30	2.8	(−3, −4)	250 ± 50	30	2
					700 ± 140	120	
NGC 7538-1[c]	23 11 36.7	61 11 51	2.8	(−1, 1)	150 ± 30	30	2
					1240 ± 250	120	
NGC 7538-9[c]	23 11 52.8	61 10 59	2.8	(3, 0)	130 ± 26	30	2
					330 ± 66	120	
S157	23 13 53.1	59 45 18	2.5	(−9, 16)	70 ± 14	30	2
					280 ± 56	120	

NOTE.—Units of right ascension are hours, minutes, and seconds, and units of declination are degrees, arcminutes, and arcseconds. Table 1 is also available in machine-readable form in the electronic edition of the *Astrophysical Journal*.

[a] 350 μm peak offset from the water maser position (0,0).

[b] The 350 μm flux density and uncertainty measured in an aperture of diameter θ_{ap}. The uncertainty is 20%. For sources with no reported 120″ aperture flux density, either the source was very weak (IRAS 02395+6244, IRAS 02461+6147, and G137.07−3.00), or the source was very centrally peaked and all of the flux is within a 30″ aperture (G12.21−0.10 and G45.07+0.13).

[c] Previously studied by van der Tak et al. 2000.

[d] Double or multiple peaks in 350 μm map.

REFERENCES.—(1) Yang et al. 1991. (2) Plume et al. 1992. (3) Plume et al. 1997. (4) Palagi et al. 1993. (5) Zhou, Evans, & Wang 1996. (6) Olmi & Cesaroni 1999. (7) Val'tts et al. 2000. (8) Zinchenko et al. 1994. (9) Hunter et al. 2000. (10) Churchwell, Wolfire, & Wood 1990. (11) van der Tak et al. 2000. (12) Mitchell, Hasegawa, & Schella 1992.

transition ($T_A^* > 1.0$ K; Plume et al. 1992). The critical density of CS $J = 5 \rightarrow 4$ is $n_c = 8.9 \times 10^6$ cm^{-3}; however, a density, $n_{\rm eff}$, of 2.2×10^6 cm^{-3} will produce an observable line of 1 K for a gas temperature of 10 K (Evans 1999). For a gas temperature of 100 K, which may better describe massive cores, the effective critical density is even lower, $n_{\rm eff} = 6.0 \times 10^4$ cm^{-3} (Evans 1999). Consequently, models constrained by multiple transitions are needed to determine density. Plume et al. (1997) reported $\langle \log n \rangle = 5.9$ from LVG models of multiple CS transitions for the regions from which our sample was taken. Therefore, these objects were known to contain a significant amount of dense gas; however, their mass and density structures were not well known. Many (43%) of the regions in our study were also known to be associated with UCH II regions.

The sample covers a large range of distances, from Ori-IRc2 at a distance of 450 pc to G12.21−0.10 at 13.7 kpc. The distances were found in the literature (see Table 1), and spectrophotometric distances were used when available. The mean distance in the sample is 3.9 kpc, while the median distance is 2.8 kpc. Figure 1 shows the distribution of distances in the sample.

Our sample includes nine objects described in van der Tak et al. (2000). The van der Tak et al. (2000) sources were selected to be luminous, visible from the Northern Hemisphere, and, in most cases, bright in the mid-infrared. For comparison, the high-mass protostellar objects studied by Beuther et al. (2002) were selected from objects north of -20° declination detected in CS $J = 2 \rightarrow 1$ (Bronfman, Nyman, & May 1996), with FIR colors characteristic of

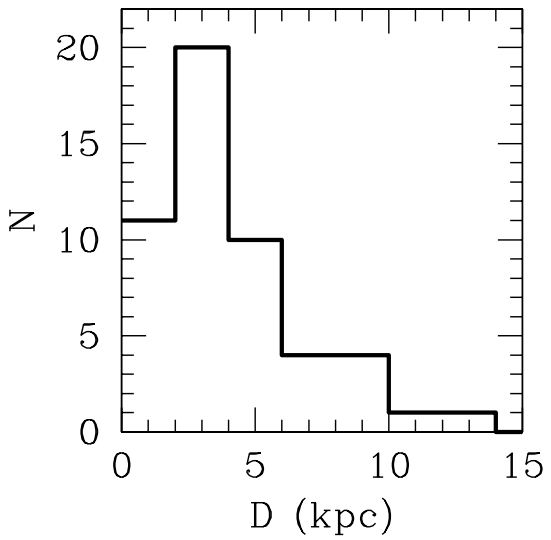

FIG. 1.—Distribution of distances in our sample. N is the number of sources.

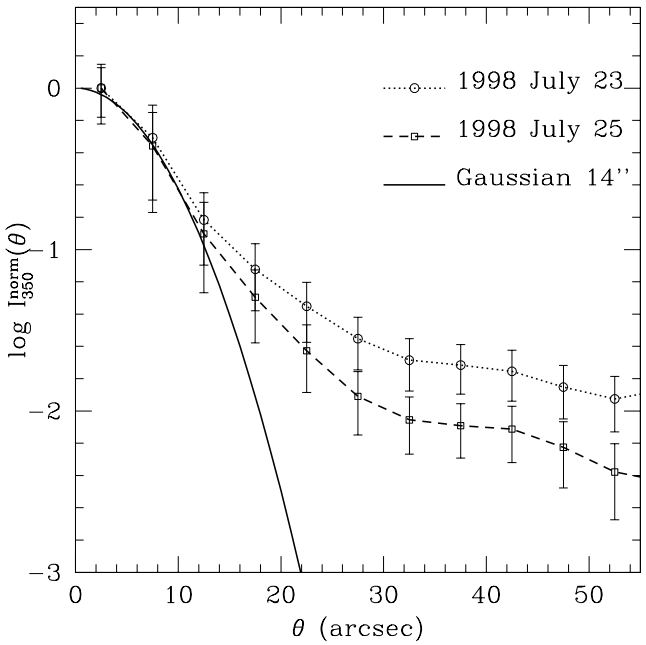

FIG. 2.—Radial profiles of Uranus on 1998 July 23 and 1998 July 25 used to measure the beam plotted with a 14″ Gaussian. The error bars represent the weighted mean variation in the annulus for which each point of the profile is calculated. We adopt an FWHM beam size, θ_{mb}, of 14″.

UCH II regions. Their sources are also bright at FIR wavelengths. However, the sources in the Beuther et al. (2002; also Sridharan et al. 2002) sample were also chosen to have low radio continuum flux (<25 mJy; Sridharan et al. 2002) to ensure that their sources were isolated and *not* typical UCH II regions. Surprisingly, our sample has only two objects in common with that of Beuther et al. (2002; S231 and G12.89+0.49).

2. OBSERVATIONS

2.1. *Observation Techniques*

Fifty-one regions forming massive stars were observed with the Submillimeter High Angular Resolution Camera (SHARC), described by Hunter, Benford, & Serabyn (1996), during five nights in 1997 (December 21 and 22) and 1998 (July 15, 23, and 25) on the 10.4 m Caltech Submillimeter Telescope. SHARC is a one-dimensional bolometer array with an FWHM beam size, θ_{mb}, of 14″ (see Fig. 2 and § 2.3).

SHARC's linear array consists of 24 detectors (Hunter et al. 1996); therefore, the telescope must be scanned in azimuth at constant elevation to map the source. Each 350 μm map consists of approximately 11 scans extending 240″ in azimuth scanning at a rate of 4″ s^{-1}. The individual scans are shifted by 4″ in elevation to extend the mapped region and to eliminate gaps in the map due to bad pixels (pixels 1, 5, 15, and 16 of the 24 pixels in the SHARC array). The scanning rate and elevation shifts were selected to be slightly smaller than the size of the pixel, 5″ in the focal plane of the array, to obtain better sampling (Hunter et al. 1996). The secondary was chopped at 1.123 Hz with a chop throw of 90″–100″ in the azimuth direction. SHARC observations were conducted only during very dry conditions with $\tau_{CSO} < 0.06$ (see § 2.3).

2.2. *Image Reduction*

All of the data were reduced and restored with the standard program CAMERA. The restoration algorithm is based on a technique described by Emerson, Klein, & Haslam (1979). The despiking routine was used on those maps that had pixels with spikes above 10 σ, which we identified by visual inspection during reduction. The routine replaces the spiked pixel with the average value of the adjacent pixels. In some cases the source was highly peaked, so a higher σ was used to ensure that the central pixel was not removed by the despiking routine. The night of 1998 July 15 was unusually windy. Five maps made on this night (W28A2, G12.89+0.49, G12.21−0.10, G24.49−0.04, W43S) showed signs of being affected by the wind and were corrected with linear destriping. The destriping affected the maximum pixel value, in most cases decreasing it by less than 10%.

After the data were reduced with CAMERA, gray-scale images of the restored and combined bolometer maps were created. The Image Reduction and Analysis Facility (IRAF) was used to find the value of the maximum pixel, the average background, and σ for each map. The voltages in each map were multiplied by the extinction correction,

$$V_{corr} = V_{obs} e^{\tau \sec z}, \quad (1)$$

where $\sec z$ is the average air mass at the time of observation. The determination of τ is described in § 2.3.

Figures 3–7 show the dust continuum contour maps. The contour levels are even multiples of σ or 10% or 20% of the peak signal with an additional lowest contour at 3 σ. The (0, 0) position is the location of the water maser from Plume et al. (1992, 1997). The positions of known UCH II regions are indicated by plus signs on the contour maps. Three of the 22 marked UCH II regions (G12.21−0.10, G23.95+0.16, and W43S) were listed as UCH II regions by Wood & Churchwell (1989) but, in the same study, were reported to have diameters greater than 0.1 pc. Therefore, these sources may also be classified as *compact* H II regions.

Normalized radial intensity profiles were created as in Shirley et al. (2000). The intensity was azimuthally averaged

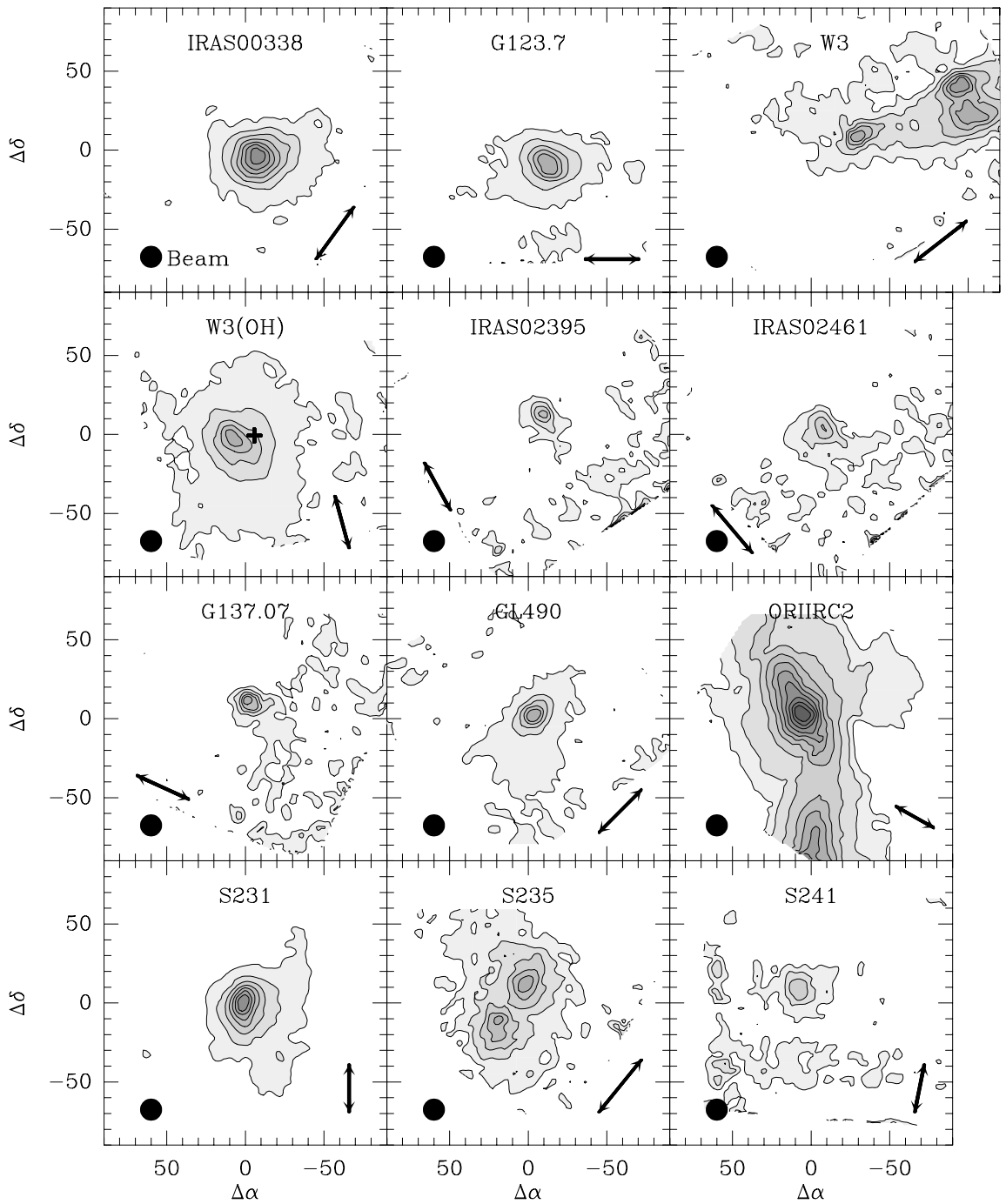

FIG. 3.—350 μm dust emission contour maps. The arrows indicate the chop direction but are not indicative of the chop length ($\sim$100″). The plus signs indicate the positions of known UCH II regions [W3(OH): Wilner et al. 1995]. The contour levels are as follows: IRAS 00338+6312 (4 σ), G123.07−6.31 (3 σ, then in increments of 20% [10 σ] of the peak), W3 (4 σ), W3(OH) (3 σ, 20% [10 σ]), IRAS 02395+6244 (2 σ), IRAS 02461+6147 (2 σ), G137.07−3.00 (2 σ), GL 490 (3 σ, 20% [6 σ]), Ori-IRc2 (3 σ, 10% [7 σ]), S231 (4 σ), S235 (2 σ), S241 (2 σ).

and normalized to the peak emission. The normalized intensities, $I(b)/I(0)$, were plotted versus the impact parameter, $b = \theta D$, a line of sight offset from the center by an angle θ, for a source at distance D. The radial profiles are truncated at a radius, $r_{\rm prof}$, when the signal fell to 1 σ or at 60″, whichever is smaller. We do not consider data beyond a 60″ radius where simulation in our models of the effects of chopping becomes problematic. Photometry was also provided by the radial profile program. The sky-subtracted fluxes for 30″ and 120″ diameter apertures, $\theta_{\rm ap}$, are listed in Table 1.

2.3. *Calibration*

The extinction coefficients at 350 μm, τ_{350}, were determined using skydips from the CSO tipper ($\tau_{\rm CSO}$) at 225 GHz. A scaling between $\tau_{\rm CSO}$ and τ_{350} has been determined by comparing skydips between the 225 GHz and 350 μm tippers,

$$\tau_{350} = (23.5 \pm 0.2)\tau_{\rm CSO} \quad (2)$$

(R. Chamberlin 2000, private communication). To check

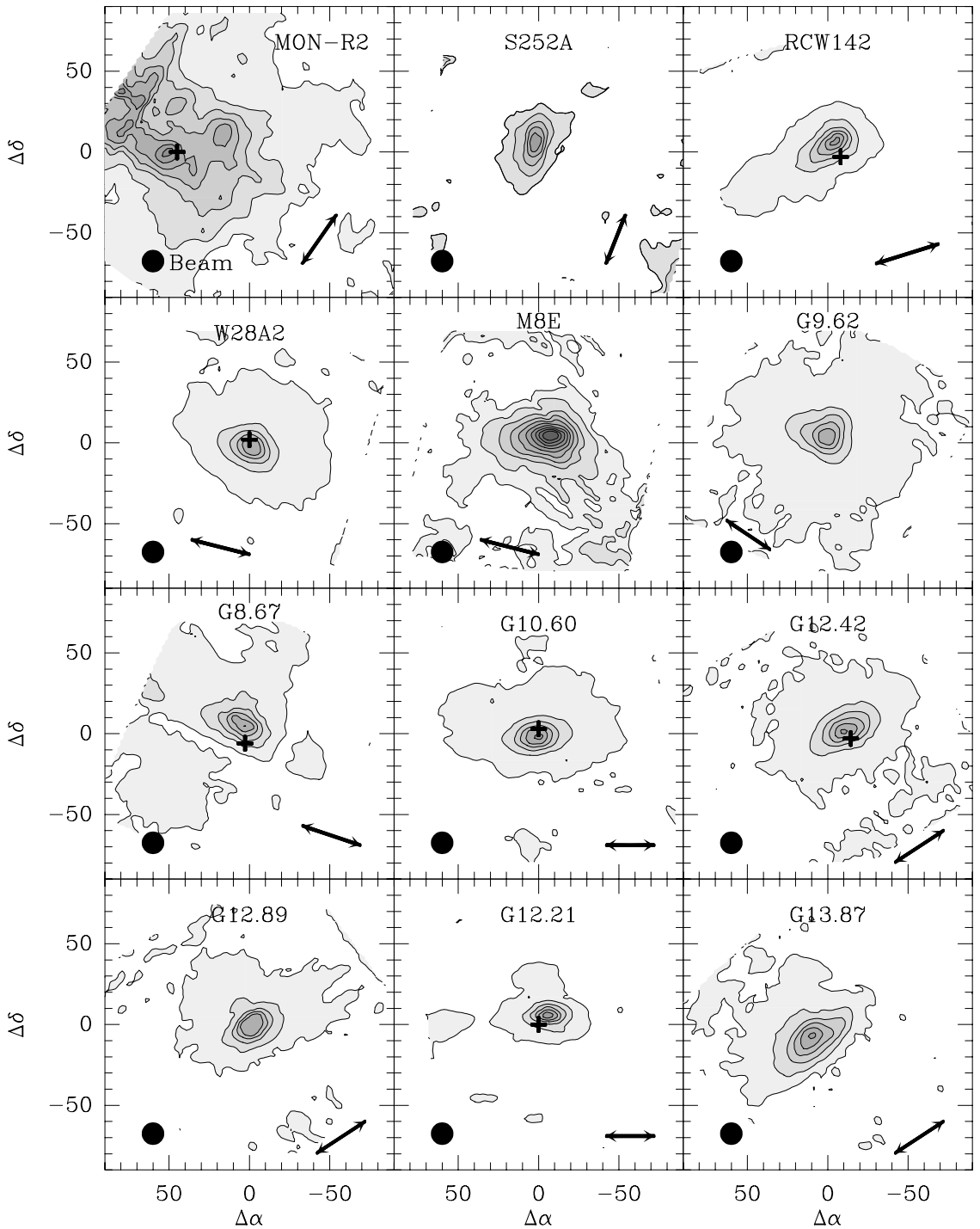

FIG. 4.—350 μm dust emission contour maps. The arrows indicate the chop direction but are not indicative of the chop length ($\sim$100″). The plus signs indicate the positions of known UCH II regions (Mon R2, W28A2, G8.67, G10.60, G12.21: Wood & Churchwell 1989; RCW 142: Walsh et al. 1998; G12.42: Jaffe et al. 1984). The contour levels are as follows: Mon R2 (4 σ), S252A (4 σ), RCW 142 (3 σ, then in increments of 20% [26 σ] of the peak), W28A2 (3 σ, 20% [29 σ]), M8E (3 σ, 10% [5 σ]), G9.62+0.10 (3 σ, 20% [28 σ]), G8.67−0.36 (3 σ, 20% [25 σ]), G10.60−0.40 (3 σ, 20% [30 σ]), G12.42+0.50 (3 σ, 20% [17 σ]), G12.89+0.49 (3 σ, 20% [12 σ]), G12.21−0.10 (3 σ, 10% [20 σ]), G13.87+0.28 (3 σ, 10% [9 σ]).

the relationship between τ_{350} and $\tau_{\rm CSO}$, Uranus was observed as it set during two nights in 1998 July with exceptionally stable sky opacity ($\sigma_\tau/\langle\tau\rangle \leq 0.06$). The variation of peak voltage on Uranus with air mass determined τ_{350}. The resulting τ_{350} was consistent with equation (2). Since we were unable to observe a source as it set during each night, and since τ_{350} may vary throughout the night, we determined the extinction correction, equation (1), for each image by scaling from $\tau_{\rm CSO}$ measurements using equation (2).

Full maps of Uranus and secondary calibrator sources, NGC 2071IR and W3(OH), were used to determine the calibration factors, C^{θ}, for each observing run. Sky subtractions were made for each image by measuring the voltage ($V_{\rm sky}$)

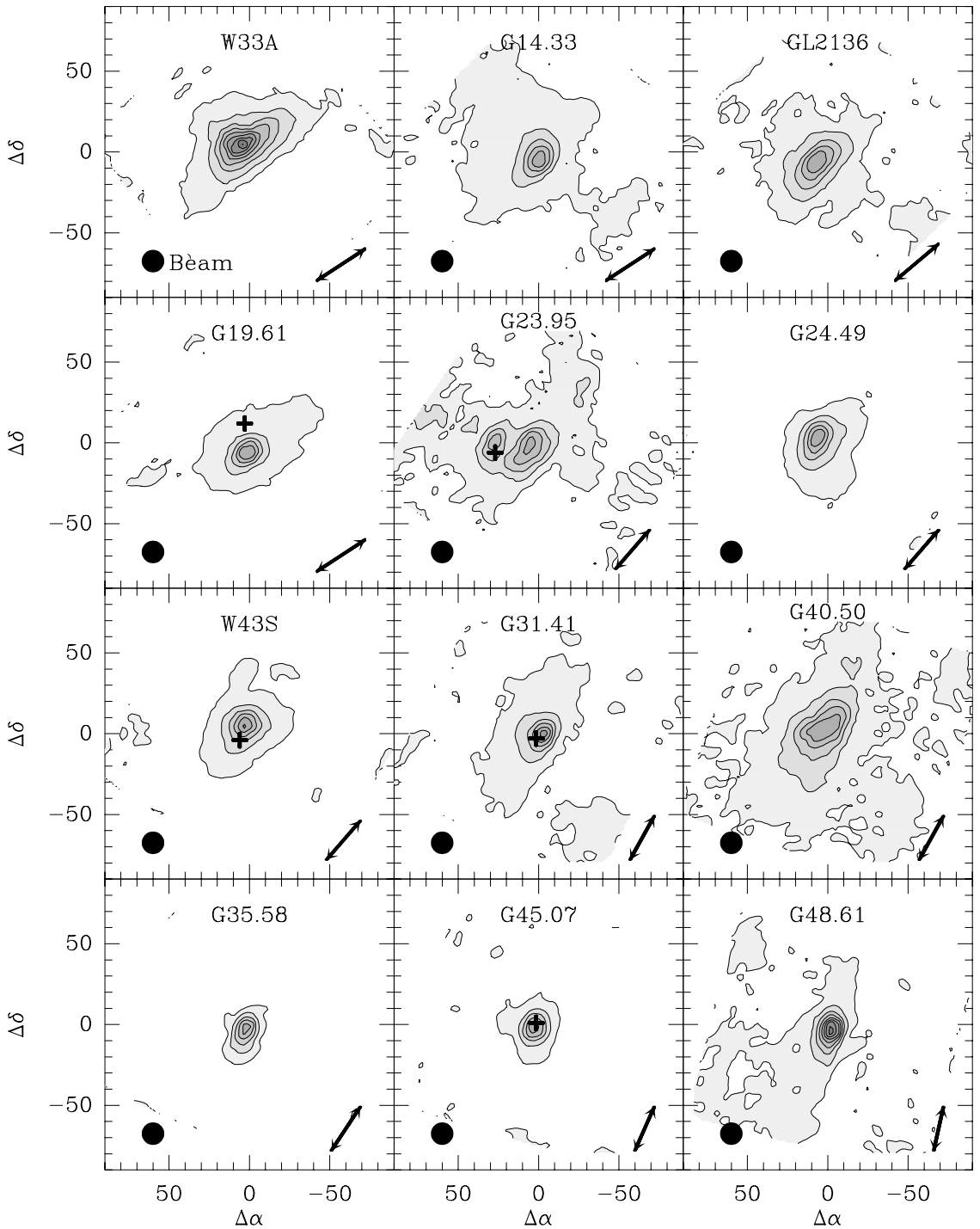

FIG. 5.—350 μm dust emission contour maps. The arrows indicate the chop direction but are not indicative of the chop length ($\sim$100″). The plus signs indicate the positions of known UCH II regions (Wood & Churchwell 1989). The contour levels are as follows: W33A (4 σ), G14.33−0.64 (3 σ, then in increments of 20% [17 σ] of the peak), GL 2136 (3 σ, 20% [8 σ]), G19.61−0.23 (3 σ, 20% [33 σ]), G23.95+0.16 (3 σ, 20% [5 σ]), G24.49−0.04 (3 σ, 20% [15 σ]), W43S (3 σ, 20% [29 σ]), G31.41+0.31 (3 σ, 20% [18 σ]), G40.50+2.54 (3 σ, 20% [10 σ]), G35.58−0.03 (4 σ), G45.07+0.13 (3 σ, 20% [6 σ]), G48.61+0.02 (3 σ, 10% [5 σ]).

through multiple 20″ apertures ($\theta_{\rm sky}$) away from the source and averaging the measured sky voltage.

Total voltages measured in apertures of diameter $\theta_{\rm ap}$ were then corrected for sky emission by

$$V(\theta_{\rm ap})_{\rm corr} = V(\theta_{\rm ap})_{\rm obs} - V_{\rm sky}\frac{\pi\theta_{\rm ap}^2}{\pi\theta_{\rm sky}^2} \ . \qquad (3)$$

The calibration factors C^{θ} were calculated for images taken in the 1998 July run by measuring the flux at 350 μm in 30″ and 120″ diameter apertures of two maps of Uranus. The total flux of Uranus in 1998 July was 266.5 Jy. Calibration factors for sources observed in 1998 July were, with statistical errors, $C^{30} = (9.6 \pm 1.5)$ mJy V^{-1} and $C^{120} = (8.5 \pm 2.0)$ mJy V^{-1} for 30″ and 120″ apertures, respectively. Because no planets were visible to serve as

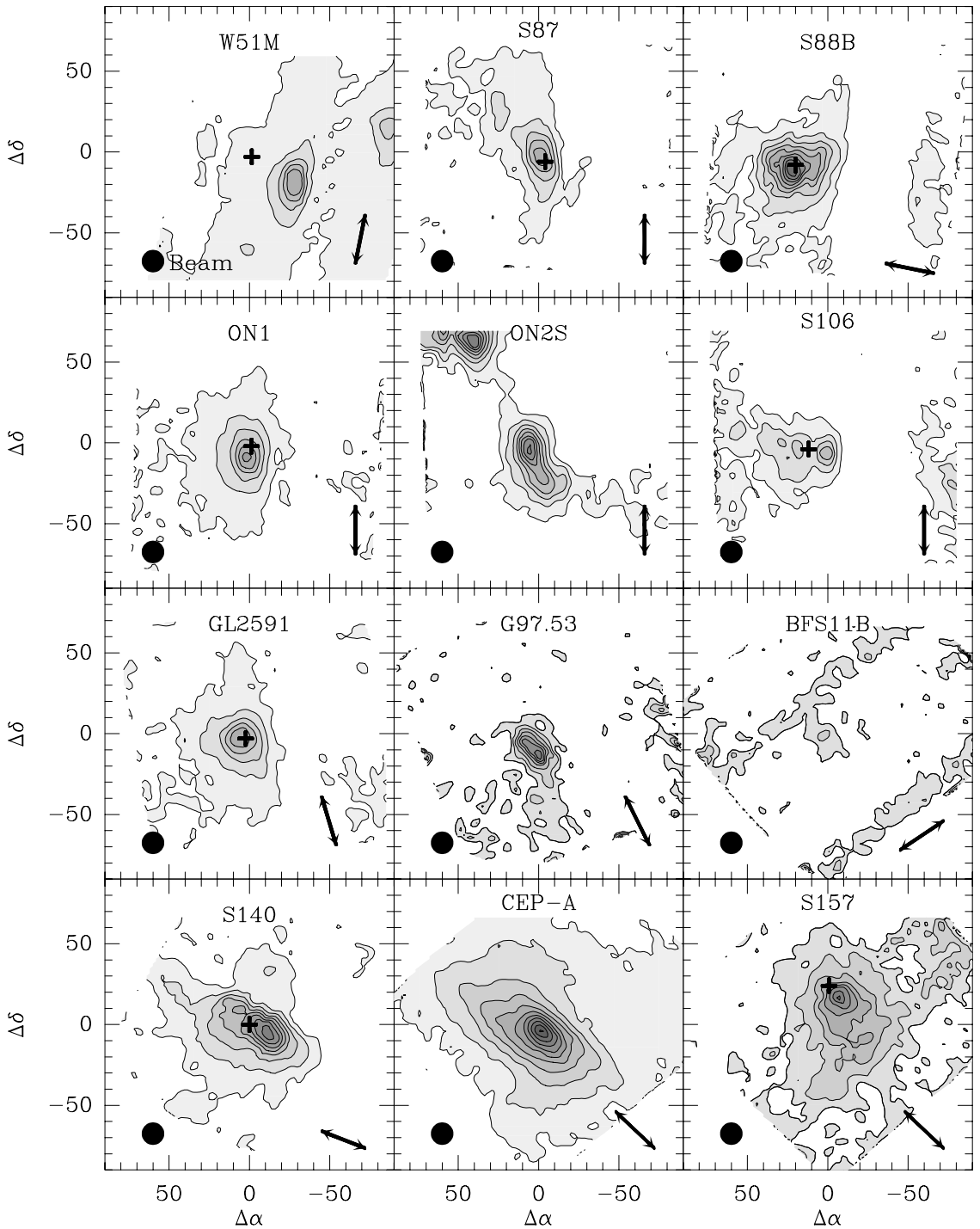

FIG. 6.—350 μm dust emission contour maps. The arrows indicate the chop direction but are not indicative of the chop length ($\sim$100″). The plus signs indicate the positions of known UCH II regions (W51M: Scott 1978; S88B: Wood & Churchwell 1989; S87, ON 1, S106, S157: Kurtz, Churchwell, & Wood 1994; GL 2591, S140: Tofani et al. 1995). The contour levels are as follows: W51M (3 σ, then in increments of 20% [19 σ] of the peak), S87 (4 σ), S88B (4 σ), ON 1 (3 σ, 20% [11 σ]), ON 2S (4 σ), S106 (4 σ), GL 2591 (3 σ, 20% [11 σ]), G97.53+3.19 (2 σ), BFS 11-B (2 σ), S140 (4 σ), CEP A (3 σ, 10% [7 σ]), S157 (2 σ).

pointlike sources in 1997 December, maps of NGC 2071IR and W3(OH) were used for calibration. The assumed fluxes for NGC 2071IR and W3(OH) were 177 and 498 Jy beam^{-1}, respectively (Sandell 1994). Voltages measured in 30″ and 120″ apertures in three maps of each secondary calibrator were used to determine calibration factors. The 1997 December calibration factors averaged over the six maps were, with statistical errors, $C^{30} = (9.6 \pm 1.3)$ mJy V^{-1} and $C^{120} = (4.7 \pm 0.7)$ mJy V^{-1}. While some of the statistical uncertainties are smaller than 20%, we expect systematic errors to not allow fluxes to be determined at 350 μm to better than 20% (Hunter et al. 2000). Furthermore, calibrations in 1997 December determined from NGC 2071IR and W3(OH) are expected to be worse since neither calibrator is a point source [see Fig. 3 for a map of W3(OH)]. This effect is obvious in C^{120}, which is nearly a factor of 2 lower when

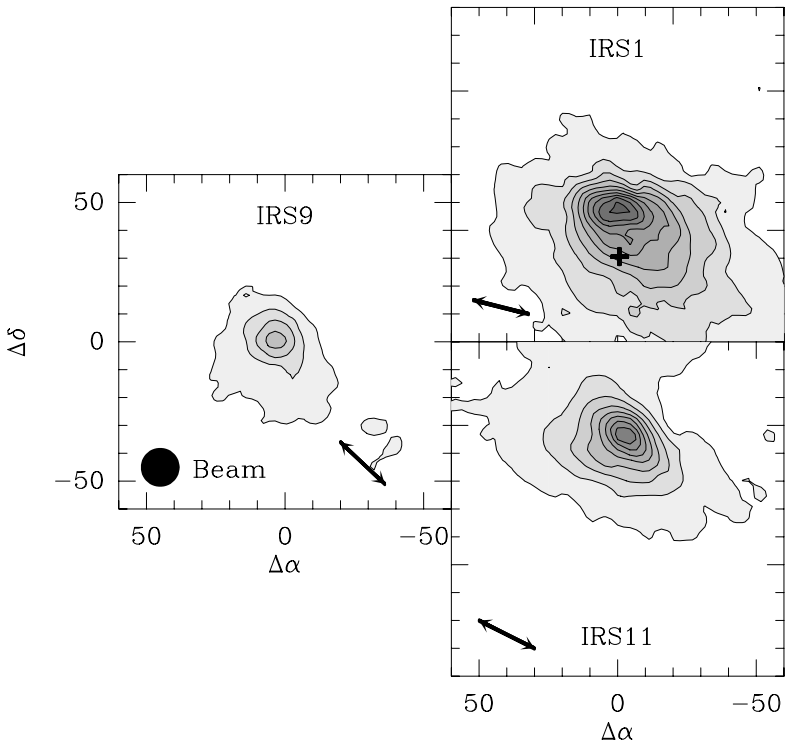

FIG. 7.—Composite 350 μm contour map of NGC 7538. The arrows indicate the chop direction but are not indicative of the chop length ($\sim$100″). Clockwise from left are the sources IRS 9, IRS 1, and IRS 11. The visible H II region NCG 7538 (S158) lies north of IRS 1. The plus sign indicates the position of the UCH II region associated with IRS 1 ($23^{h}11^{m}36\overset{s}{.}6$, $61^{\circ}11'36\overset{''}{.}6$; Wood & Churchwell 1989). The contour levels are as follows: IRS 9 (4 σ), IRS 1 (3 σ, 10% [6 σ]), IRS 11 (3 σ, 10% [6 σ]).

using the secondary calibrators. C^{30} was not affected by the extended emission and is stable from 1997 December to 1998 July. For this reason, C^{120} from 1998 July is used to calibrate all of the 120″ aperture fluxes.

Radial beam profiles were obtained from two maps of Uranus in 1998 July (Fig. 2). The data were binned in 5″ bins. Broad sidelobes are seen beyond 15″. At 40″, the sidelobe power is as high as -17 dB. The general shape of the two profiles is consistent, but there are variations in the strength of the sidelobes. Fitting the beam profiles with a Gaussian, we find that the FWHM is at least 14″, which is significantly different from the beam size reported in previous studies using SHARC at 350 μm (10″, van der Tak et al. 2000; 11″, Hunter et al. 2000). The difference could be the result of poor focus or temporal changes in the beam. Young et al. (2003) report a 3″ change in the FWHM of the James Clerk Maxwell Telescope beam at 450 μm in the course of a single night. The beam measurements were not frequent enough to characterize the changes of the CSO beam over the course of the observations in this study; therefore, we adopt $\theta_{\rm mb} = 14''$.

3. RESULTS

Most of the cores appear slightly elongated in the contour maps (Figs. 3–7). This is likely an effect of chopping during observations as the maps are usually elongated along the chop direction. The chop direction is indicated on the maps with an arrow. However, some of the sources have extended asymmetrical emission at 350 μm distinct from the chopping asymmetry with an intensity of a few σ (e.g., ON 2S, G40.50+2.54). Some (14%) of the maps have double or multiple peaks, indicating the presence of more than one luminosity source. These sources are noted in Table 1. A few have close embedded double peaks (e.g., G23.95+0.16, S235), while others show more spatially distinct peaks. For example, the NGC 7538 region shows three distinct peaks in Figure 7; these were mapped separately but are plotted in their relative locations.

The contour maps also show that the 350 μm dust peak is often nearly coincident with the water maser position at the center of the map. Thirty cores (59%) have the dust centroid within $\theta_{\rm mb}/2$ of the maser position (see Table 1). The mean absolute distance of the dust centroid to the maser position is 8″. About half of the 22 known UCH II regions in the sample are also close ($<\theta_{\rm mb}/2$) to the maser; however, the mean absolute distance of the UCH II position from the water maser is 10″. This separation is similar to that of the UCH II region from the dust peak with mean absolute distance of 11″. Samples based on water masers favor an earlier phase of star formation than UCH II region samples (Cesaroni et al. 1988; Shirley et al. 2002a). The high coincidence of the dust centroid and maser position in these regions implies that the dust emission may be primarily tracing the earlier stages as well.

The FWHM size of each source, $\theta_{\rm dec}$, was determined by deconvolving the telescope main beam from the observed FWHM of the core by subtracting $\theta_{\rm mb}$ from the observed FWHM in quadrature. The observed FWHM was determined from the radial profile of each source. The deconvolved half-power radius is defined to be $r_{\rm dec} = (D/2)\theta_{\rm dec}$, where D is the distance to the source. For the entire sample, $\langle r_{\rm dec}\rangle = 0.16 \pm 0.10$ pc, with a median of 0.14 pc. Figure 8 shows the distribution of $r_{\rm dec}$.

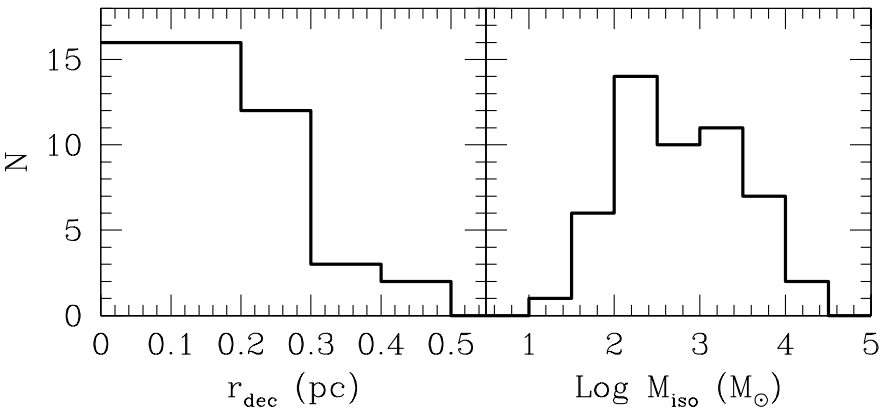

FIG. 8.—Distribution of radii and masses for the complete sample; $r_{\rm dec}$ is the deconvolved half-power size as determined from the 350 μm dust emission and $M_{\rm iso}$ is the isothermal mass.

Photometry from the literature is collected in Table 2. The observed spectral energy distribution (SED) was used to calculate the bolometric luminosity, $L_{\rm bol}$, for each source, using only data taken with beam sizes $\geq 20''$, with the exception of the endpoints to the SED. Luminosities range over 3 orders of magnitude, about 10^3–10^6 $L_\odot$ with $\langle L_{\rm bol}\rangle = 2.5 \times 10^5$ $L_\odot$ and a median $L_{\rm bol} = 5.1 \times 10^4$ $L_\odot$. If all the luminosity is attributed to a single star, the range of spectral types would be B3–O4, with the median being an O9 star. Considering multiple sources and accretion luminosity would lower these spectral types.

Many recent studies have used power laws to fit directly the radial intensity profiles and infer the density structure of star-forming regions (e.g., Shirley et al. 2000; Beuther et al. 2002). We did not use this technique; however, for comparison purposes, we describe some general trends in the radial profiles of our sample. Generally, the radial profiles follow a power law from about $12''$ (approximately $\theta_{\rm mb}$) to $40''$. The profiles are flattened toward the interior, and beyond $40''$, they sometimes deviate from the power law. The flattening at small angles is likely due to beam effects but could also result from fragmentation of the core. The change in the slope beyond $40''$ is not consistently steeper or shallower. Some radial profiles are distorted by the presence of multiple peaks.

4. MODELS

One of the major motivations for this study was to learn what density distributions fit the data. A power-law density distribution was assumed of the form $n(r) = n_f(r/r_f)^{-p}$, for p in a range of 0.5–2.5. We chose $r_f = 1000$ AU for convenient comparison to other studies, but this r_f is well inside our beam. The values of n_f should be taken only as indicative of likely mean densities as substructure is very likely on those scales. The observed radial intensity profiles and SEDs were modeled using a modified version of the one-dimensional dust continuum radiative transfer code by Egan, Leung, & Spagna (1988) and an observation simulation code described by Evans et al. (2001). The radiative transfer code calculates the radial temperature distribution, $T_D(r)$, self-consistently for each input model of $n(r)$.

We also included contributions from the interstellar radiation field (ISRF) to the temperature distribution at the edge of the cloud. Figure 9 shows that $T_D(r)$ is approximately a power law. At small radii, $T_D(r)$ deviates by rising more steeply toward the center than a strict power law. Additionally, the ISRF causes an upturn in $T_D(r)$ at large radii (about 1 pc for a 10^4 $L_\odot$ source). The ISRF makes a substantial contribution to the temperature profile in regions forming low-mass stars where the internal luminosity is low (Shirley et al. 2002b; Young et al. 2003) but has little effect in regions forming massive stars because the temperature profile is dominated by the embedded source. While these sources may exist in regions of enhanced ISRF, the effects on the models are negligible even in our least luminous sources ($L_{\rm bol} = 10^3$ $L_\odot$) unless the ISRF is a factor of 10 stronger than the standard value (see Evans et al. 2001 for a plot of the ISRF). For a more typical source with $L_{\rm bol} = 10^4$ $L_\odot$, the ISRF field must be at least 200 times stronger to change the best-fit p by 0.25.

For each of our models, the input density, n_f, was normalized so that the model flux at 350 μm matched our observations, given a dust opacity at 350 μm. Dust opacities were adopted from column (5) of Table 1 in Ossenkopf &

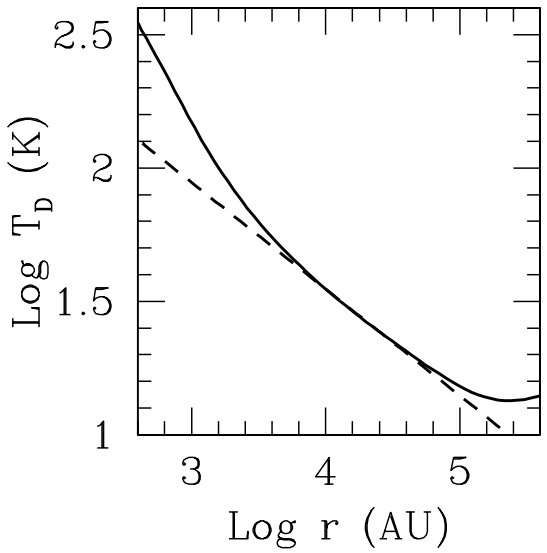

FIG. 9.—Model dust temperature distribution for internal source with $L_{\rm bol} = 10^4$ $L_\odot$ (*solid line*) and a $T_D(r) \propto r^{-0.4}$ power law (*dashed line*). The modeled distribution deviates from a strict power law at large r because of the ISRF and at small r because of optical depth effects.

TABLE 2

COLLECTED PHOTOMETRY

Source	λ (μm)	S_ν[a] (Jy)	Beam[b] (arcsec)	Reference
IRAS 00338+6312	12[c]	1.8 ± 0.2	300 × 45	1
	25[c]	21 ± 1	300 × 45	1
	60[c]	357 ± 21	90 × 300	1
	100[c]	685 ± 55	180 × 300	1
	143[c]	1615 ± 323	105	2
	185[c]	2317 ± 463	102	2
	350[c]	160 ± 32	30	...
	350	410 ± 82	120	...
	350	111 ± 5	19	3
	450[c]	49 ± 2	18	3
	450	66 ± 1.5	8	4
	800[c]	6.2 ± 0.02	16	3
	850[c]	6.6 ± 0.07	14.5	4
	850	17 ± 3.4	18	5
	1100[c]	2.3 ± 0.044	18.7	3
	1100	5.6 ± 1.1	18	6
G123.07−6.31	12[c]	<1.8	300 × 45	1
	25[c]	13 ± 1	300 × 45	1
	60[c]	330 ± 46	90 × 300	1
	100[c]	1166 ± 117	180 × 300	1
	350[c]	160 ± 32	30	...
	350	290 ± 58	120	...
W3	40	800 ± 80	49	7
	350	2400 ± 1200	15	8
	350	30 ± 6	30	...
	350	220 ± 44	120	...
	400	500 ± 50	49	7
	800	160 ± 32	19	8
	1100	20 ± 3	19	8
W3(OH)	20[c]	270 ± 27	49	7
	25[c]	670 ± 67	49	7
	30[c]	1400 ± 140	49	7
	35	25502 ± 55	49	7
	40[c]	4000 ± 400	49	7
	40	4000 ± 100	49	9
	50	5600 ± 560	49	7
	58	6500 ± 480	50	9
	60[c]	7000 ± 700	49	7
	70[c]	8500 ± 850	49	7
	80	9300 ± 930	49	7
	85	9500 ± 440	50	9
	90[c]	9400 ± 940	49	7
	100[c]	9000 ± 900	49	7
	120	8000 ± 800	49	7
	138	6900 ± 450	50	9
	140[c]	6700 ± 670	49	7
	160	5800 ± 580	49	7
	180[c]	4900 ± 490	49	7
	200[c]	4100 ± 410	49	7
	250[c]	2400 ± 240	49	7
	300[c]	1400 ± 140	49	7
	350	400 ± 80	30	...
	350[c]	1130 ± 230	120	...
	400	520 ± 52	49	7
	500[c]	250 ± 25	49	7
	600[c]	135 ± 14	49	7
	800[c]	51 ± 5.1	49	7
	1000[c]	24 ± 2.4	49	7
IRAS 02395+6244	12	11 ± 0.4	300 × 45	1
	25	92 ± 3.7	300 × 45	1
	60	255 ± 23	90 × 300	1
	100	226 ± 38	180 × 300	1
	350	20 ± 4	30	...
IRAS 02461+6147	12	10 ± 0.8	300 × 45	1
	25	84 ± 5	300 × 45	1
	60	291 ± 26	90 × 300	1
	100	373 ± 52	180 × 300	1
	350	20 ± 4	30	...
G137.07−3.00	12	0.35 ± 0.03	300 × 45	1
	25	<0.25	300 × 45	1
	60	<0.40	90 × 300	1
	100	<12	180 × 300	1
	350	20 ± 4	30	...
GL 490	12	82 ± 2.5	300 × 45	1
	25	278 ± 8.3	300 × 45	1
	60	717 ± 29	90 × 300	1
	100	785 ± 55	180 × 300	1
	350	80 ± 16	30	...
	350	180 ± 36	120	...
	870	12 ± 1.2	14	10
	1300	3.6 ± 0.2	14	10
Ori-IRc2	12	120 ± 14	2.3	11
	20	240 ± 29	2.3	11
	57	113000 ± 11000	180	12
	138	219000 ± 22000	180	12
	205	26000 ± 2600	180	12
	350	1940 ± 390	30	...
	350	7680 ± 1540	120	...
S231	12[c]	5.6 ± 0.2	300 × 45	1
	25[c]	75 ± 3.7	300 × 45	1
	60[c]	722 ± 72	90 × 300	1
	100[c]	1310 ± 131	180 × 300	1
	350[c]	190 ± 38	12	...
	350	522 ± 100	120	...
S235	10[c]	37 ± 7	60	13
	12	28 ± 1.7	300 × 45	1
	20[c]	340 ± 70	60	13
	25	226 ± 13.6	300 × 45	1
	50[c]	695 ± 140	37	13
	60	179 ± 171	90 × 300	1
	100	1635 ± 164	180 × 300	1
	100[c]	740 ± 150	37	13
	350[c]	50 ± 10	30	...
	350	240 ± 48	120	...
S241	12	1.9 ± 0.3	300 × 45	1
	25	11.8 ± 0.7	300 × 45	1
	60	<189	90 × 300	1
	100	552 ± 77	180 × 300	1
	350	30 ± 6	30	...
	350	40 ± 8	120	...
Mon R2	12	470 ± 14	300 × 45	1
	20	500 ± 250		14
	20	2275		14
	25	4095 ± 164	300 × 45	1
	27	5866		14
	40	12976		14
	60	13070 ± 1961	90 × 300	1
	93	18825		14
	100	20200 ± 3030	180 × 300	1
	140	7200		14
	200	3300 ± 830	60	9
	350	150 ± 30	30	...
	350	1400 ± 280	120	...
	390	660		14
	850	21 ± 4	18	15
	1000	58		14
	1300	16.64 ± .76	30	16
S252A	12[c]	16 ± 0.6	300 × 45	1
	25[c]	77 ± 3	300 × 45	1
	60[c]	10321 ± 34	90 × 300	1
	100[c]	1715 ± 189	180 × 300	1
	350[c]	130 ± 26	30	...
	350	320 ± 64	120	...
RCW 142	12[c]	<42	300 × 45	1
	25[c]	<281	300 × 45	1

TABLE 2—*Continued*

Source	λ (μm)	S_ν[a] (Jy)	Beam[b] (arcsec)	Reference
	60[c]	5476 ± 986	90 × 300	1
	100[c]	13129 ± 1313	180 × 300	1
	350[c]	530 ± 110	30	...
	350[c]	670 ± 130	120	...
W28A2	12[c]	199 ± 12	300 × 45	1
	25[c]	2190 ± 131	300 × 45	1
	60[c]	12790 ± 3198	90 × 300	1
	100[c]	26780 ± 6695	180 × 300	1
	350	830 ± 166	11	17
	350[c]	950 ± 190	30	...
	350[c]	1580 ± 320	120	...
M8E.....	10	87	4	18
	12	119 ± 7	300 × 45	1
	20	178	4	18
	25[c]	289 ± 17	300 × 45	1
	60[c]	1611 ± 226	90 × 300	1
	64	≤3600	210	19
	69[c]	2600	54	20
	100[c]	2783 ± 696	180 × 300	1
	110	10000 ± 3000	210	19
	160	5200 ± 1600	210	19
	350[c]	210 ± 42	30	...
	350[c]	380 ± 76	120	...
	450[c]	42 ± 15.8	19	21
	850[c]	9 ± 1.01	25	21
G9.62+0.10	12[c]	39 ± 2.3	300 × 45	1
	25[c]	292 ± 18	300 × 45	1
	60[c]	4106 ± 411	90 × 300	1
	100[c]	7844 ± 1098	180 × 300	1
	350[c]	590 ± 120	30	...
	350[c]	1150 ± 230	120	...
	1300[c]	9.6	90	22
	2700[c]	0.0098	3	23
G8.67−0.36.....	12	19 ± 1	300 × 45	1
	25[c]	254 ± 8	300 × 45	1
	60[c]	1895 ± 303	90 × 300	1
	100[c]	5125 ± 1128	180 × 300	1
	350[c]	650 ± 130	30	...
	350[c]	1160 ± 230	120	...
	450[c]	390 ± 98	18	5
	850[c]	49 ± 10	18	5
	1300[c]	7.1	90	22
G10.60−0.40.....	12[c]	<23	300 × 45	1
	18	3.1 ± 0.3	29	24
	25[c]	<148	300 × 45	1
	60[c]	9479 ± 948	90 × 300	1
	69[c]	14000	90	25
	100[c]	21375 ± 3847	180 × 300	1
	350[c]	1110 ± 220	30	...
	350[c]	1900 ± 380	120	...
	1300[c]	26	90	26
G12.42+0.50.....	12	10.7 ± 1.1	300 × 45	1
	20[c]	100 ± 10	49	27
	25	253 ± 15.2	300 × 45	1
	40[c]	760 ± 76	49	27
	59[c]	1490 ± 149	49	27
	60	1418 ± 255	90 × 300	1
	100	2380 ± 595	180 × 300	1
	101[c]	24202 ± 42	49	27
	135[c]	2270 ± 227	49	27
	180[c]	2100 ± 210	49	27
	350[c]	210 ± 42	30	...
	350[c]	440 ± 88	120	...
	400[c]	160 ± 16	49	27
G12.89+0.49.....	12	<6.1	300 × 45	1
	20[c]	30 ± 3	49	27
	25	45 ± 4.5	300 × 45	1
	40[c]	360 ± 36	49	27

TABLE 2—*Continued*

Source	λ (μm)	S_ν[a] (Jy)	Beam[b] (arcsec)	Reference
	59[c]	1100 ± 110	49	27
	60	1248 ± 225	90 × 300	1
	100	3148 ± 787	180 × 300	1
	101[c]	2200 ± 220	49	27
	135[c]	2370 ± 237	49	27
	180[c]	2370 ± 237	49	27
	350[c]	220 ± 44	30	...
	350[c]	340 ± 68	120	...
	400[c]	210 ± 21	49	27
	450[c]	200 ± 50	18	14
G12.21−0.10.....	20[c]	40 ± 4	49	7
	40[c]	420 ± 42	49	7
	59[c]	810 ± 81	49	7
	101[c]	2500 ± 250	49	7
	165[c]	1550 ± 155	49	7
	350	560 ± 112	11	17
	350[c]	230 ± 46	30	
	400[c]	80 ± 8	49	7
	450[c]	94 ± 19	9	28
	850[c]	14 ± 0.7	15	28
	1350[c]	3.2 ± 0.6	22	28
	2000[c]	1.1 ± 0.2	34	28
G13.87+0.28.....	12	75 ± 4.5	300 × 45	1
	25[c]	478 ± 29	300 × 45	1
	60[c]	3632 ± 509	90 × 300	1
	100	<6141	180 × 300	1
	350[c]	190 ± 38	30	...
	350[c]	430 ± 86	120	...
	450[c]	24 ± 5	9	28
	850[c]	5.2 ± 0.3	15	28
	1300	7.3	90	26
	1350[c]	2.2 ± 0.4	22	28
	2000[c]	1.50 ± .2	34	28
W33A	12.5	22 ± 3	9	29
	20	50 ± 20	9	29
	20[c]	113 ± 11	49	7
	20	113 ± 5	6.8	30
	25[c]	371 ± 21	6.8	30
	25	268 ± 21	300 × 45	1
	33[c]	539 ± 36	6.8	30
	40[c]	1000 ± 100	49	7
	42[c]	1300 ± 130	60	31
	59[c]	2350 ± 235	49	7
	60	2206 ± 530	90 × 300	1
	73[c]	3400 ± 340	60	31
	77[c]	4100 ± 410	60	31
	101[c]	4050 ± 405	49	7
	100	6183 ± 1422	180 × 300	1
	135[c]	3900 ± 390	49	7
	135	4000 ± 400	60	1
	180[c]	2750 ± 275	49	7
	350[c]	350 ± 70	30	...
	350[c]	960 ± 190	120	...
	400[c]	300 ± 30	49	2
	450[c]	240 ± 60	18	32
	850[c]	45 ± 9	18	32
	1000[c]	41 ± 8	65	33
	1300[c]	11	90	22
	1300	7.3	90	26
	1300	3.0	30	32
G14.33−0.64.....	12	<6.4	300 × 45	1
	20	40 ± 4	49	27
	25	56 ± 5.6	300 × 45	1
	40[c]	400 ± 40	49	27
	59[c]	740 ± 74	49	27
	60	994 ± 249	90 × 300	1
	100	2819 ± 705	180 × 300	1
	101[c]	2000 ± 200	49	27

TABLE 2—*Continued*

Source	λ (μm)	S_ν[a] (Jy)	Beam[b] (arcsec)	Reference
	135[c]	2000 ± 200	49	27
	180[c]	2300 ± 230	49	27
	350[c]	440 ± 88	30	...
	350[c]	830 ± 170	120	...
	400[c]	120 ± 12	49	27
GL 2136	11[c]	40 ± 8	180	34
	350[c]	240 ± 48	30	...
	350[c]	520 ± 100	120	...
	450[c]	72 ± 6	19	35
	800[c]	7.1 ± 0.2	17	35
	800	6.7 ± 0.2	17	35
	1100[c]	2.4 ± 0.04	19	35
	1100	2.4 ± 0.09	19	35
	1300[c]	1.7 ± 0.05	19	35
	2000[c]	0.5 ± 0.12	19	35
G19.61−0.23	12	48 ± 4.3	300 × 45	1
	18	103 ± 10	29	24
	25	407 ± 32.6	300 × 45	1
	60	4635 ± 417	90 × 300	1
	100	7093 ± 922	180 × 300	1
	350	460 ± 92	30	...
	350	500 ± 200	120	...
G23.95+0.16	12[c]	66.3 ± 1.2	300 × 45	1
	25[c]	395 ± 6.2	300 × 45	1
	60[c]	2285 ± 708	90 × 300	1
	100[c]	3339 ± 902	180 × 300	1
	350	105	22	36
	350[c]	100 ± 20	30	...
	350[c]	320 ± 64	120	...
	800[c]	14.5	50	36
	1300[c]	4.6	90	22
G24.49−0.04	12[c]	15.5 ± 2.2	300 × 45	1
	25[c]	81 ± 8.1	300 × 45	1
	60[c]	1476 ± 88	90 × 300	1
	100[c]	3514 ± 14	180 × 300	1
	350[c]	190 ± 37	30	...
	350[c]	190 ± 37	120	...
W43S	12[c]	218 ± 20	300 × 45	1
	12.5[c]	235	22	37
	12.6	121	2	37
	19[c]	610	12	37
	25[c]	1697 ± 136	300 × 45	1
	60[c]	7501 ± 525	90 × 300	1
	100[c]	11669 ± 3151	180 × 300	1
	350[c]	360 ± 72	30	...
	350[c]	440 ± 88	120	...
	1300[c]	8	90	22
	1300	20 ± 1.9	12	38
G31.41+0.31	12	4 ± 0.4	300 × 45	1
	25[c]	52 ± 5.2	300 × 45	1
	60[c]	1093 ± 197	90 × 300	1
	100[c]	2815 ± 394	180 × 300	1
	350	997 ± 200	11	1
	350[c]	460 ± 92	30	...
	350[c]	740 ± 150	120	...
	450[c]	84 ± 17	9	28
	850[c]	27 ± 1.4	15	28
	1300	14	90	22
	1350[c]	4.9 ± 1.0	22	28
	2000[c]	2.9 ± 0.6	34	28
G40.50+2.54	12[c]	31.8 ± 4.5	300 × 45	1
	25[c]	242 ± 24	300 × 45	1
	60[c]	2351 ± 423	90 × 300	1
	100[c]	4218 ± 840	180 × 300	1
	350[c]	240 ± 48	30	...
	350[c]	600 ± 120	120	...
	450[c]	215 ± 54	18	5
	850[c]	33 ± 7	18	5

TABLE 2—*Continued*

Source	λ (μm)	S_ν[a] (Jy)	Beam[b] (arcsec)	Reference
G35.58−0.03	12	<6.0	300 × 45	1
	25	77 ± 3.9	300 × 45	1
	60	1507 ± 196	90 × 300	1
	100	2594 ± 571	180 × 300	1
	350	110 ± 22	30	...
	350	120 ± 24	120	...
G45.07+0.13	12	58 ± 3.5	300 × 45	1
	25	494 ± 30	300 × 45	1
	60	<5913	90 × 300	1
	100	<7497	180 × 300	1
	350	180 ± 36	30	...
G48.61+0.02	12[c]	<25	300 × 45	1
	25[c]	175 ± 10	300 × 45	1
	60[c]	3195 ± 320	90 × 300	1
	100[c]	5227 ± 523	180 × 300	1
	350[c]	100 ± 20	30	...
	350[c]	200 ± 40	120	...
W51M	12	424 ± 42	300 × 45	1
	25	4344 ± 430	300 × 45	1
	100	< 26760	180 × 300	1
	350	280 ± 56	30	...
	350	3690 ± 740	120	...
	1300	27 ± 2.7	25	39
S87	12	47 ± 3.8	300 × 45	1
	25	425 ± 26	300 × 45	1
	60	3446 ± 310	90 × 300	1
	100	5158 ± 464	180 × 300	1
	350	140 ± 28	30	...
	350	310 ± 62	120	...
	450	110 ± 28	18	5
	850	17 ± 3	18	5
	1300	3.6	90	22
S88B	10.2	0.04 ± 0.01	17	40
	11.1	0.12 ± 0.024	17	40
	12[c]	93 ± 6.5	300 × 45	1
	12.6[c]	22 ± 4.4	17	40
	17[c]	40 ± 8.0	17	40
	25[c]	1185 ± 71.1	300 × 45	1
	60[c]	8686 ± 1129	90 × 300	1
	100[c]	13214 ± 1057	180 × 300	1
	350[c]	150 ± 30	30	...
	350[c]	540 ± 110	120	...
	1300[c]	3.4	90	22
ON 1	12[c]	1.1 ± 0.1	300 × 45	1
	25[c]	58.8 ± 4.7	300 × 45	1
	60[c]	1431 ± 115	90 × 300	1
	100[c]	3119 ± 312	180 × 300	1
	350[c]	320 ± 64	30	...
	350[c]	650 ± 130	120	...
ON 2S	12	330		41
	12[c]	74 ± 4.5	300 × 45	1
	25[c]	481 ± 29	300 × 45	1
	60	4200		41
	60[c]	5446 ± 545	90 × 300	1
	100	13000		41
	100[c]	<6985	180 × 300	1
	350[c]	200 ± 40	30	...
	350[c]	510 ± 100	120	...
	1300[c]	9	90	26
S106	12	204 ± 12	300 × 45	1
	25	2510 ± 176	300 × 45	1
	60	10100 ± 1111	90 × 300	1
	100	13100 ± 1179	180 × 300	1
	350	110 ± 22	30	...
	350	400 ± 80	120	...
GL 2591	12	439 ± 26.3	300 × 45	1
	12.6	680	6.6	15
	19.5[c]	630	6.6	15

TABLE 2—*Continued*

Source	λ (μm)	S_ν[a] (Jy)	Beam[b] (arcsec)	Reference
	23[c]	920	6.6	15
	25	1112 ± 67	300 × 45	1
	60[c]	4600 ± 920	49	15
	60	5314 ± 425	90 × 300	1
	95[c]	5800 ± 300	49	15
	100	5721 ± 858	180 × 300	1
	110[c]	5500 ± 1100	49	15
	160[c]	34006 ± 80	49	15
	350[c]	230 ± 46	30	...
	350[c]	440 ± 88	120	...
	450[c]	170 ± 43	18	5
	850[c]	19 ± 4	18	5
	1300[c]	5.7 ± 1.57	30	16
	1300	2.49	30	32
	3300[c]	0.115 ± 0.034	75	42
G97.53+3.19	350	50 ± 10	30	...
	350	90 ± 18	120	...
BFS 11-B	25	79 ± 5	300 × 45	1
	60	688 ± 76	90 × 300	1
	100	1215 ± 97	180 × 300	1
	175	410 ± 110		14
	350	40 ± 8	30	...
	350	90 ± 18	120	...
	450	60 ± 15		14
	800	4.2 ± 8		14
	1100	1.2		14
S140	10	150 ± 38	3.5	43
	12[c]	332 ± 40	30	43
	20[c]	740 ± 185	3.5	43
	25[c]	1694 ± 170	30	43
	35[c]	5700 ± 1425	34	43
	53[c]	8200 ± 2050	17	43
	60	11374 ± 1200	60	43
	62[c]	7600 ± 130	49	43
	76[c]	9200 ± 150	49	43
	80[c]	9900 ± 2475	37	43
	100	8600 ± 2150	38	43
	100	13000 ± 1300	120	43
	101[c]	7700 ± 150	49	43
	111[c]	7500 ± 150	49	43
	162[c]	4700 ± 120	49	43
	175[c]	54001 ± 350	45	43
	350	333 ± 50	30	32
	350[c]	350 ± 70	30	...
	350[c]	1210 ± 240	120	...
	400[c]	3508 ± 8	49	43
	1300[c]	1.4 ± 0.25	30	32
	1300	15.9	30	16
CEP A	12[c]	170 ± 60	300 × 45	1
	20	416 ± .2	4	44
	25[c]	860 ± 215	300 × 45	1
	30	27 ± 5.65	30	16
	50[c]	10600 ± 2650	20	44
	60[c]	17000 ± 3400	90 × 300	1
	85	46500 ± 12900	270	45
	100[c]	230004 ± 600	180 × 300	1
	100[c]	20200 ± 5050	30	44
	125[c]	33100 ± 9170	50	46
	150	23400 ± 6800	270	45
	350[c]	430 ± 86	30	...
	350[c]	1500 ± 300	120	...
	400[c]	2570 ± 741	50	46
	450[c]	737 ± 140	20	47
	550	27900 ± 6300	50	46
	800[c]	86 ± 10	20	47
	865	84 ± 18	8	48
	1300[c]	26 ± 8	40	48
	1300	27 ± 1.6	30	16

TABLE 2—*Continued*

Source	λ (μm)	S_ν[a] (Jy)	Beam[b] (arcsec)	Reference
S158	12	243 ± 7.3	300 × 45	1
	25	1780 ± 71	300 × 45	1
	60	7073 ± 495	90 × 300	1
	100	14138 ± 1131	180 × 300	1
	350	249 ± 50	30	49
	350	250 ± 50	30	...
	350	700 ± 140	120	...
	1300	15	30	49
NGC 7538-1	12.5[c]	149 ± 21	7.5	1
	20[c]	250 ± 50	6	50
	25[c]	640 ± 130	6	50
	30[c]	2300 ± 700	40	50
	50[c]	6700 ± 2010	40	50
	100[c]	11000 ± 3300	55	50
	350[c]	150 ± 30	30	...
	350[c]	1240 ± 250	120	...
	1000[c]	30 ± 9	55	50
NGC 7538-9	12.5[c]	74 ± 13	9	50
	20[c]	124 ± 30	6	50
	25[c]	260 ± 50	6	50
	30[c]	500 ± 150	40	50
	50[c]	1300 ± 390	40	50
	100[c]	2700 ± 810	55	50
	350[c]	130 ± 26	30	...
	350[c]	330 ± 66	120	...
	1000[c]	51 ± 5	55	50
S157	12[c]	29 ± 3	300 × 45	1
	25[c]	233 ± 12	300 × 45	1
	60[c]	1759 ± 123	90 × 300	1
	100[c]	264 ± 303	180 × 300	1
	350[c]	70 ± 14	30	...
	350	280 ± 56	120	...
	850[c]	5.9 ± 1.2	18	5

NOTE.—Table 2 is also available in machine-readable form in the electronic edition of the *Astrophysical Journal*.

[a] Observed flux density and uncertainty. 350 μm flux densities with beam = 30″ or 120″ are from this work.

[b] FWHM beam size for observed flux density.

[c] Flux value used in model.

REFERENCES.—(1) *IRAS* PSC 1988. (2) Mookerjea et al. 1999. (3) Dent, Matthews, & Ward-Thompson 1998. (4) Sandell & Weintraub 2001. (5) Jenness, Scott, & Padman 1995. (6) McCutcheon et al. 1995. (7) D. Jaffe 2001, private communication. (8) Richardson et al. 1989. (9) Thronson et al. 1980. (10) Chini, Henning, & Pfau 1991. (11) Gezari, Backman, & Werner 1998. (12) Mookerjea et al. 2000. (13) Evans et al. 1981a. (14) Jenness 1996. (15) Lada et al. 1984. (16) Walker, Adams, & Lada 1990. (17) Hunter et al. 2000. (18) Simon et al. 1985. (19) Thronson, Lowenstein, & Stokes 1979. (20) Wright et al. 1977. (21) Tothill 1999. (22) Chini et al. 1986a. (23) Hofner et al. 1996. (24) De Buizer 2000. (25) Fazio et al. 1978. (26) Chini et al. 1986b. (27) Jaffe et al. 1984. (28) Hatchell et al. 2000. (29) Evans et al. 1979. (30) Dyck & Simon 1977. (31) Stier 1984. (32) Guertler et al. 1991. (33) Cheung et al. 1980. (34) Lebofsky et al. 1976. (35) Kastner et al. 1994. (36) Hoare, Roche, & Glencross 1991. (37) Soifer & Pipher 1975. (38) Mooney et al. 1995. (39) Schloerb, Snell, & Schwartz 1987. (40) Pipher et al. 1977. (41) Dent, MacDonald, & Anderson 1988. (42) Schwartz & Spencer 1977. (43) Zhou et al. 1994. (44) Ellis et al. 1990. (45) Koppenaal et al. 1979. (46) Evans et al. 1981b. (47) Moriarity-Schieven, Snell, & Hughes 1991. (48) Gordon 1990. (49) Chini, Kruegel, & Kreysa 1986c. (50) Werner et al. 1979.

Henning (1994, hereafter OH5), which were calculated for coagulated dust grains with ice mantles. These dust opacities (OH5) have been previously shown to match observations of massive star formation regions by van der Tak et al. (1999, 2000) as well as low-mass star-forming regions (Evans et al. 2001; Shirley et al. 2002b; Young et al. 2003).

We also considered opacities for grains without ice mantles taken from column (2) of Table 1 in Ossenkopf & Henning (1994; OH2) because temperatures in regions with young stars may be high enough to destroy the mantles. The OH2 opacities are higher at $\lambda > 350$ μm ($\kappa_{\rm OH2}/\kappa_{\rm OH5} = 1.8$ at 700 μm) but lower at shorter wavelengths. The crossover point is near 350 μm, with $\kappa_{\rm OH2}/\kappa_{\rm OH5} = 1.1$ at 350 μm (see Fig. 2 of Evans et al. 2001). Using OH2 opacities thus results in best-fit n_f lower by about 10%. Using OH2 opacities also resulted in higher model fluxes at long wavelengths but lower fluxes at short wavelengths. No difference was found in the best-fit p between the OH2 and OH5 opacities.

For each value of p and n_f, other model input parameters were adjusted to fit the observed values. The temperature of the star was taken to be the value corresponding to a star with $L = L_{\rm bol}$ (Thompson 1984). However, the results are very insensitive to the stellar temperature (van der Tak et al. 2000). The outer, r_o, and inner, r_i, radii for each source are based on the angular extent of the observed radial profile and the chopper throw. We set r_o to be the sum of the chopper throw and twice the extent of the observed profile. In particular, r_o is large enough to allow simulation of chopping. The inner model radius was taken to be r_o divided by 1000, so that it is small enough to be unresolved. The model's sensitivity to the radii was tested in M8E (see § 4.1). The best-fit values were found to be insensitive to both inner and outer radii (see § 4.1; Shirley et al. 2002b; Young et al. 2003).

The observation simulation program uses the temperature distribution output from the radiative transfer code for the density model being tested. The code calculates observed fluxes and luminosities and generates a radial profile of normalized intensity. The model is convolved with the observed beam and chopping is simulated to produce a more realistic radial profile for comparison with observations. For our models, an average one-dimensional representation of the actual beam was used (Fig. 2). The fit of the models with the observations was quantified by calculation of the reduced χ^2 (χ^2_r). The χ^2_r value for the radial profile follows the definition in Evans et al. (2001) and is denoted χ^2_{350}. We also compute a χ^2_r value for the fit to the SED, denoted $\chi^2_{\rm SED}$. The shortest wavelength point was generally left out of the calculation of $\chi^2_{\rm SED}$ because the model underestimates the flux at $\lambda \leq 30$ μm. This effect is well known in spherical models that do not account for holes and inhomogeneities in the cloud that allow these wavelengths to escape (e.g., van der Tak et al. 2000).

The modeling scheme and the dependence of the derived quantities on the model parameters are discussed by Evans et al. (2002), and the sensitivity of the best-fit p to uncertainties in other parameters is quantified for low-luminosity regions by Shirley et al. (2002b). They found that the largest source of uncertainty in p is the strength of the ISRF. For the luminous sources studied here, this is a minor source of uncertainty, as already noted.

4.1. *M8E: A Model in Detail*

M8E was used as a test case for checking the effects of the input parameters on the models. The 350 μm contour map of M8E is shown in Figure 4. A spectrophotometric distance of 1.8 kpc (Blitz, Fich, & Stark 1982) was used. The observed bolometric luminosity, $L_{\rm bol}$, was 1.47×10^4 $L_\odot$. The best-fit model yielded $L_{\rm bol} = 1.45 \times 10^4$ $L_\odot$, calculated from convolving the model emission with the beams used for the observations. The sensitivity of the model to the input internal luminosity was tested by decreasing and increasing the parameter by a factor of 2. While changing the luminosity affected the model SED by increasing or decreasing the flux at certain wavelengths, it had no effect on the radial profile fit.

The fiducial density, n_f, was fixed by matching the model flux at 350 μm to the observed value for each modeled density distribution. The best-fit $n_f = 1.2 \times 10^7$ cm^{-3} for M8E. For M8E, $r_o = 4.3 \times 10^5$ AU (2.1 pc) and $r_i = 430$ AU. To test the sensitivity of the models to these parameters, r_i was doubled and, independently, r_o was halved. Both tests yielded the same best-fit p as the model with r_i and r_o calculated in the standard way. Other resulting model values, such as $L_{\rm bol}$ and $T_{\rm bol}$, also did not vary significantly. Therefore, we concluded that the models are insensitive to changes of a factor of 2 in r_i and r_o.

Figure 10 shows the best-fit model for this source, a density power law with $p = 1.75$ ($\chi^2_{\rm SED} = 13.5$, $\chi^2_{350} = 0.52$). As with a few sources of our sample, the best-fit density distribution to the radial profile did not agree with the best fit to

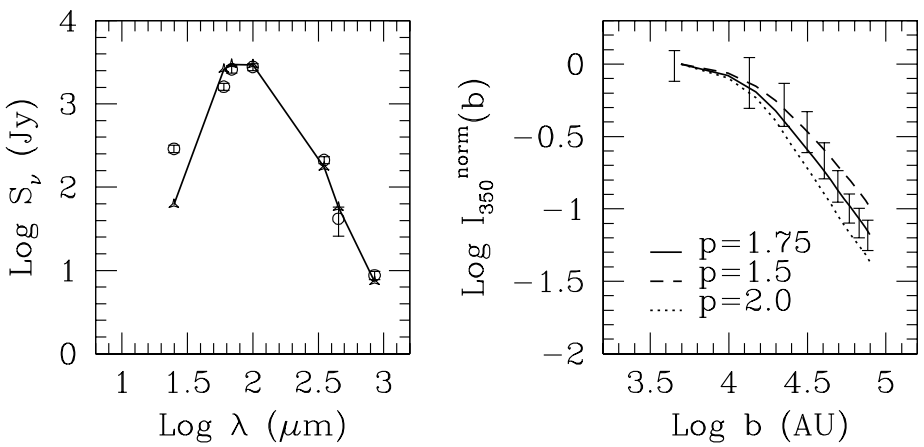

FIG. 10.—*Left:* Observed (*circles with error bars*) and best-fit model (*solid line*) SED ($\chi^2_R = 14$) for M8E. *Right:* Best-fit model for the observed normalized radial intensity profile (*error bars*), $p = 1.75$ (*solid line*, $\chi^2_R = 0.52$). The error bars in the radial profile represent the weighted mean variation in the annulus for which each point of the profile is calculated. Also plotted are the $p = 1.5$ (*dashed line*, $\chi^2_R = 4.3$) and $p = 2.0$ (*dotted line*, $\chi^2_R = 3.4$) model profiles.

the SED for M8E. The $\chi^2_{\rm SED}$ was lower (8.3) with $p = 1.5$ and a lower fiducial density and central temperature. However, the slope of the model radial profile is clearly too shallow ($\chi^2_{350} = 4.3$, shown as a dashed line in Fig. 10). With M8E and the other sources that showed a disagreement in the best fit of the SED and radial profile, we report the best-fit p to the radial profile because the shape of the opacity law and density inhomogeneities strongly affect the SED at wavelengths where the dust is optically thick. The radial profiles are much more effective in constraining the value of p. The $p = 2.0$ model (Fig. 10, *dotted line*) produced a slope very similar to what was observed but was not a best fit because the radial profile steepens at a smaller radius than observed.

These models illustrate (Fig. 10) a conservative uncertainty in p of ± 0.25; while $p = 1.5$ and 2 clearly do not fit the data as well as $p = 1.75$, they do lie at the edges of the error bars in the data. The χ^2_{350} for models with $p = 1.6$–1.9 were near or less than 1. The models were quantitatively distinguishable for $\delta p = \pm 0.2$ ($\chi^2_{350} = 2.4$ for $p = 1.55$). The limiting uncertainty in p appears to be the signal-to-noise ratio of the profiles, rather than any systematic effect. However, this uncertainty assumes that a power-law density profile is a reasonable model; many sources are known to be more complex on smaller scales.

Another source of uncertainty is the knowledge of the beam profile. Shirley et al. (2002b) tested the effects of the James Clerk Maxwell Telescope (JCMT) beam uncertainties and found $\delta p = 0.1$. As were all sources, M8E was modeled with the average of the two observed beam profiles shown in Figure 2. For M8E, we also tried each of the two beam profiles, which were observed on different nights. Using the individual beam profiles did not change the result ($\delta p < 0.05$) for M8E. For these data, the beam uncertainties are negligible compared with those in the data, as long as the measured beam is used. If the beam is represented by a Gaussian, the effects are much larger (§ 6.1).

4.2. *Model Results*

Of our sample of 51 regions forming massive stars, 31 could be modeled. We required that the source was not confused with multiple sources, that the map had high signal-to-noise ratio, and that a range of flux density measurements were available in the literature. Most of our modeled sources are well resolved; i.e., the *deconvolved* source size is at least the beam size, $\theta_{\rm dec}/\theta_{\rm mb} \geq 1$. We also consider some smaller sources to be resolved and require $\theta_{\rm dec}/\theta_{\rm mb} \geq 0.8$ (or a source with an observed FWHM of 1.3 times the FWHM of the beam) for modeling. Table 3 lists $\theta_{\rm dec}/\theta_{\rm mb}$ for the sample. Three modeled sources have $0.8 < \theta_{\rm dec}/\theta_{\rm mb} < 1$ (W28A2, W43S, G31.41+0.31). The model results for these sources show steep density profiles ($p = 2.25$–2.5) and should be considered less robust than the rest of the sample because they may not be resolved as a result of uncertainties in the beam. However, the steeper profiles may also be real; in § 6.3 we discuss the correlation between p and $\theta_{\rm dec}/\theta_{\rm mb}$. Because of this correlation, our models are biased against sources with $p > 2.5$, which would not be considered resolved. The requirement on $\theta_{\rm dec}$ also produces a bias against small sources. For a source at the median distance of 2.8 kpc, sources with $r_{\rm dec} < 0.14$ pc would not qualify for modeling. If the minimum 350 μm flux density of our modeled sample and the median distance are assumed, the minimum required mass for our models is 61 $M_\odot$. The sources with small angular extents were also in some cases the most luminous and distant sources (e.g., G12.21−0.10 with $L_{\rm bol} = 5.5 \times 10^5\ L_\odot$ and $D = 13.7$ kpc).

Figures 11 and 12 show the best-fit model with the observed SED and radial profile for a subsample of sources that illustrate the full range of best-fitting p-values. Figure 13 shows a histogram of the best-fit p-values. The mean and standard deviation of the histogram are $\langle p \rangle = 1.8 \pm 0.4$. The standard deviation is about twice our estimated uncertainties on a single fit, providing marginal evidence for a range of actual values of p. Figure 13 also shows the distribution of densities at 1000 AU, n_f. For this sample, $\langle n_f \rangle = 1.2 \times 10^8$ cm^{-3} and the median value is 1.4×10^7 cm^{-3}. In § 6.3 we compare the distributions of p and n_f to those found in studies of low-mass star formation.

The models generally fit the observed radial profiles very well. The value of χ^2_{350} for the best-fit models was less than 1 for nearly all the models. The majority of the $\chi^2_{\rm SED}$ values were under 10 over the range of wavelengths where they were computed. For reasons described in § 4, the model typically underestimates the emission at shorter wavelengths, where the dust is becoming optically thick. Models with density inhomogeneities (clumps, cavities, etc.) or flattened structure might match the emission at shorter wavelengths, but such models introduce many free parameters.

Recent studies of low-mass star-forming cores using the same modeling techniques as presented here have found a correlation between p and the aspect ratio of the core (Shirley et al. 2002b; Young et al. 2003). Because our source shapes were affected by chopping, we cannot measure reliable aspect ratios in enough sources to make this comparison.

The modeled density power-law exponent can also be affected by the inclusion of a compact central source, such as a UCH II region. For low-mass star-forming cores, the inclusion of a compact source, in that case a disk, decreased p for the envelope by 0.5 (Young et al. 2003).

The UCH II region at the position of the water maser in W3(OH) has a 3 mm flux density of 3.5 Jy (Wilner, Welch, & Forster 1995). For a conservative upper limit on the amount of flux the UCH II region contributes at 350 μm, we have assumed that all of the 3 mm flux is due to ionized gas rather than dust and that the UCH II region is optically thick at 350 μm so that $S_\nu \propto \nu^2$. These assumptions give the maximum contribution of a UCH II region at 350 μm as 23% of the total observed flux. Including a compact source with this maximum contribution in our dust model, assuming that all of the emission from the UCH II region is included only in the central beam of our observations (as in Young et al. 2003), steepens the radial profile and, therefore, steepens the best-fit p to the radial profile. For W3(OH), p increased by 0.3. The result is that the possible presence of a compact source introduces uncertainty into the models because the modeled density power law of the envelope is steeper than the density structure if there were no compact source. We conclude that a UCH II region introduces uncertainty in our model results for the density structure of the envelope, $\delta p = -0.3$, if it contributes more than 20% of the total 350 μm flux.

Rick Forster at the Berkeley-Illinois-Maryland Association (BIMA) generously provided recent 3 mm flux densities for several UCH II regions near the center of cores in this study. Three of the four sources have negligible contribu-

TABLE 3
MODELED AND OBSERVED SOURCE PROPERTIES

Source	p[a]	n_f[b] ($\times 10^7$ cm^{-3})	L_{bol}[c] ($\times 10^4\ L_\odot$)	T_{bol}[d] (K)	θ_{dec}/θ_{mb}[e]
IRAS 00338+6312	1.25	0.4	0.11	46	1.6
G123.07−6.31	1.75	3.0	0.60	51	1.1
W3	...	...	2.4	77	1.0
W3(OH)	1.50	1.5	9.5	65	1.6
IRAS 02395+6244	...	...	5.6	107	0.8
IRAS 02461+6147	...	...	1.9	99	1.1
GL 490	...	...	0.24	112	1.5
Ori-IRc2	...	...	9.9	73	1.5
S231	1.50	1.0	1.3	63	1.5
S235	...	...	0.95	125	2.2
S241	...	...	1.3	62	1.0
Mon R2	...	...	3.7	98	...
S252A	1.75	1.0	0.64	68	1.0
RCW 142	2.25	6.5	5.7	64	1.0
W28A2	2.25	25	20	60	0.9
M8E	1.75	1.2	1.7	93	1.6
G9.62+0.10	2.00	17	35	68	1.1
G8.67−0.36	2.00	15	13	67	1.0
G10.60−0.40	2.50	120	92	52	1.0
G12.42+0.50	2.00	3.2	1.9	70	1.1
G12.89+0.49	2.00	5.7	3.9	56	1.0
G12.21−0.10	...	...	55	57	0.5
G13.87+0.28	1.75	2.0	13	93	1.6
W33A	1.50	2.0	10	65	1.5
G14.33−0.64	2.00	1.8	10	55	1.0
GL 2136	1.75	6.3	1.0	173	1.1
G19.61−0.23	...	...	18	74	1.1
G23.95+0.16	1.50	0.5	19	91	1.5
G24.49−0.04	2.25	8.5	4.9	65	1.1
W43S	2.50	60	160	93	0.8
G31.41+0.31	2.25	80	23	55	0.8
G40.50+2.54	1.50	0.8	2.8	75	1.6
G35.58−0.03	...	...	4.2	66	1.3
G45.07+0.13	...	...	120	79	1.3
G48.61+0.02	...	...	100	70	0.5
W51M	...	...	380	88	1.0
S87	...	...	4.8	80	1.3
S88B	1.25	0.1	9.0	75	2.8
ON 1	1.75	7.0	15	57	1.4
ON 2S	1.75	2.0	37	80	1.5
S106	...	...	50	94	0.5
GL 2591	2.00	0.9	2.0	86	1.1
BFS 11-B	...	...	0.70	64	...
S140	1.25	0.3	1.9	91	2.6
Cep A	1.50	0.5	2.2	84	1.8
S158	...	...	19	91	1.0
NGC 7538-1	1.50	1.2	15	74	1.8
NGC 7538-9	1.75	1.2	3.6	81	1.5
S157	0.75	0.01	2.9	86	3.6

[a] The best-fit model power-law density distribution exponent.
[b] The model density at 1000 AU.
[c] The bolometric luminosity calculated from the SED.
[d] The temperature of a blackbody with the same mean frequency of the SED.
[e] The ratio of the deconvolved source size to the beam size. Sources with $\theta_{dec}/\theta_{mb} < 0.8$ were not modeled.

tion from the UCH II region at 350 μm. Therefore, the simple presence of a UCH II region does not necessarily imply an uncertainty in p.

Our results for the density structure of massive star-forming regions can be compared with theoretical predictions. The mean value of p (1.8) is incompatible with a logatropic sphere ($p = 1$; McLaughlin & Pudritz 1997) at about a 2 σ level. However, both $p = 1.5$ and $p = 2$ are possible, so the inside-out collapse model of star formation (Shu 1977) cannot be ruled out. While a changing opacity as a function of radius might affect the values of p and this conclusion, the opacity of a grain with (OH5) and without

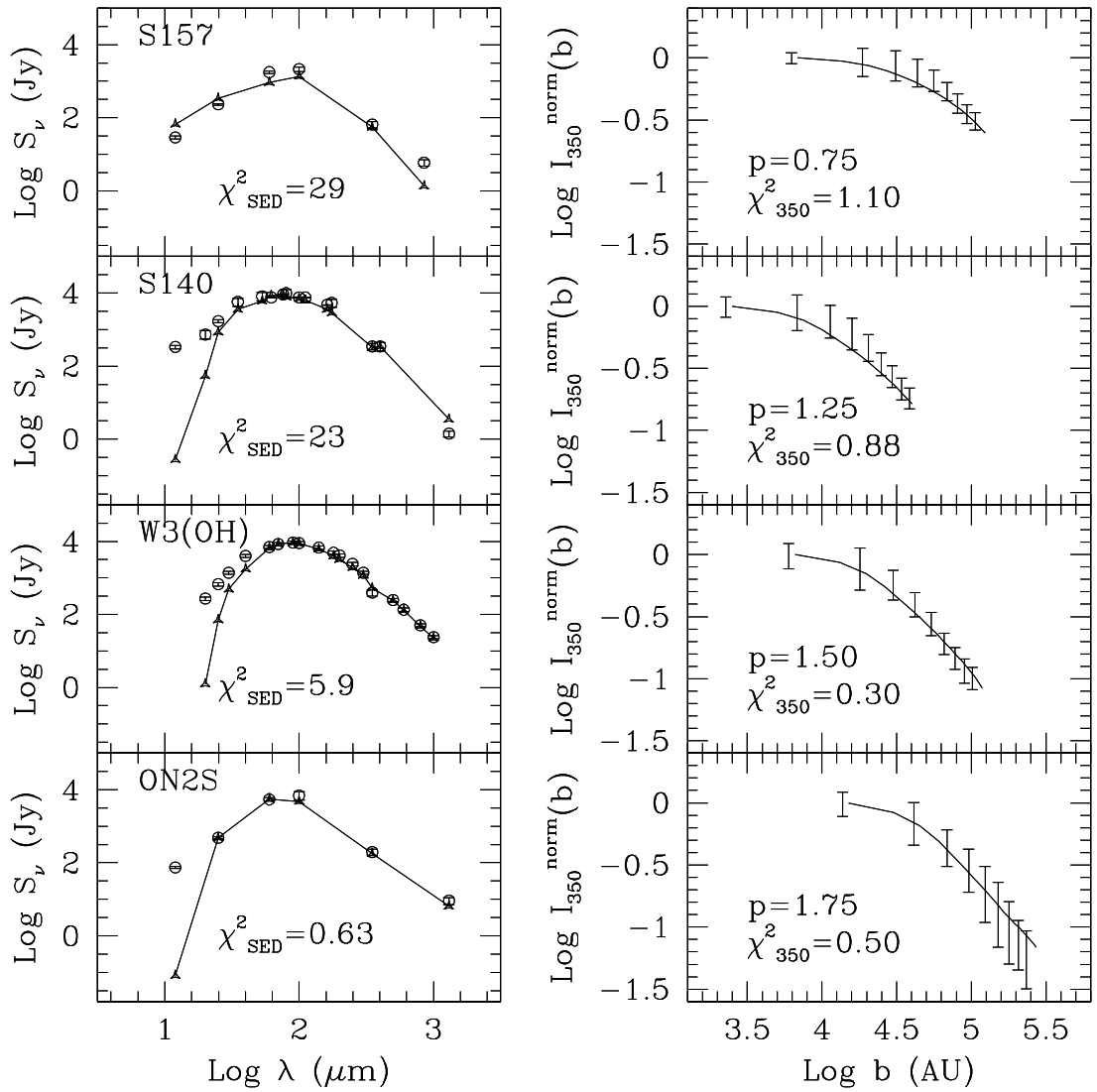

FIG. 11.—Observed SEDs (*circles*) and normalized radial profiles (*error bars*) for a subsample of sources with best-fit models (*solid line*) for $p = 0.75$–1.75. The error bars in the radial profiles represent the weighted mean variation in the annulus for which each point of the profile is calculated. χ^2_{SED} is calculated for SED points greater than 12 μm.

(OH2) an ice mantle is nearly the same at 350 μm, so evaporation of mantles will not have a large effect (see § 4).

5. MASSES

5.1. *Integrated Mass*

In a power-law mass distribution, the mass can only be defined within some specified radius. For sources with models, we can compute the integrated mass within a particular radius, R, from

$$M_{\rm int} = 4\pi\mu m n_f r_f^p \int_0^R r^{2-p}\, dr = 4\pi\mu m n_f r_f^p \frac{R^{3-p} - r_i^{3-p}}{(3-p)}\ , \quad p < 3\ , \quad (4)$$

where $\mu = 2.3$, m is the hydrogen atom mass, n_f is the gas density at r_f (1000 AU), and p is the best-fit density power-law exponent. These masses refer to the total mass of gas and dust within R. The mass is proportional to R^{3-p}; for the mean value of p, $M_{\rm int} \propto R^{1.2}$.

One choice for R is $r_{\rm dec}$, the radius corresponding to the deconvolved source size. While this size has no intrinsic meaning if the density distribution is truly a power law, it is a fiducial size that is model independent. For the modeled sample, the integrated masses (Table 4) within $r_{\rm dec}$ range from 6 to 1500 $M_\odot$ and $\langle r_{\rm dec}^{\rm mod}\rangle = 0.16 \pm 0.09$ pc, the same as for the complete sample; $\langle M(< r_{\rm dec})\rangle = 250 \pm 380\ M_\odot$ with a median value of 120 $M_\odot$, and $\langle \log M(< r_{\rm dec})\rangle = 2.0 \pm 0.6$ for this subsample.

A second, more physical choice for R is the radius inside which the density is actually enhanced over the surrounding cloud. This choice would define the total mass of the actual core, but we generally lack information for particular sources on the ambient density. In a study of extended cloud conditions in regions of massive star formation, including some studied here, K. N. Allers et al. (2002, in preparation) find a typical ambient gas density of $n \sim 10^4$ cm^{-3}. The models for cores allow determination of r_n, defined to be the

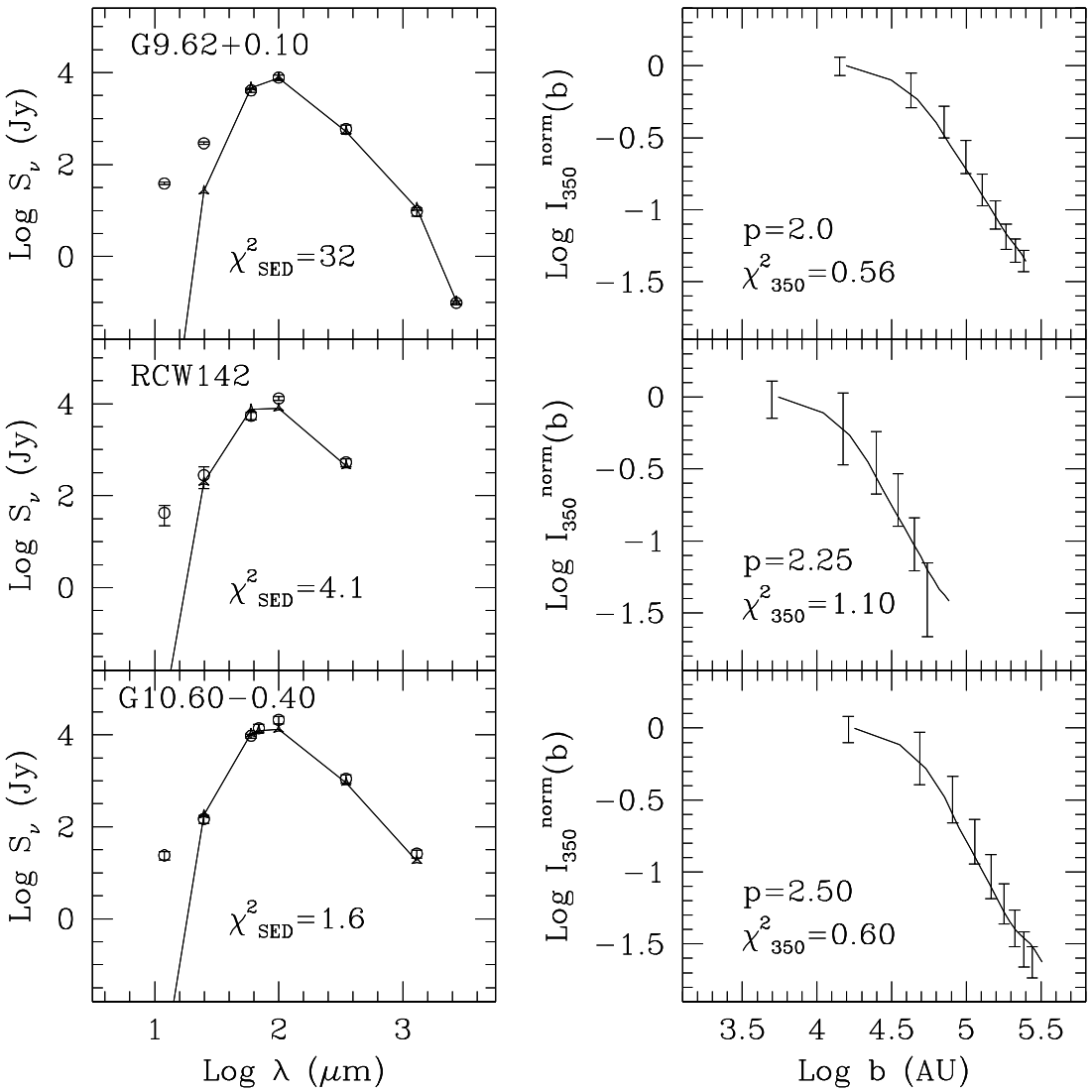

FIG. 12.—Observed SEDs (*circles*) and normalized radial profiles (*error bars*) for a subsample of sources with best-fit models (*solid line*) for $p = 2.0$–2.5. The error bars in the radial profiles represent the weighted mean variation in the annulus for which each point of the profile is calculated. χ^2_{SED} is calculated for SED points greater than 12 μm.

radius at which $n = 10^4$ cm^{-3}. For the modeled sample of 31 sources, $\langle r_n \rangle = 0.42$ pc, about 2.5 times $\langle r_{dec} \rangle$. Setting $R = r_n$ yields a core mass $[M(< r_n)]$ given in Table 4 for each core. Averaged over the cores with models, $\langle M(< r_n) \rangle = 720 \pm 860\ M_\odot$ and $\langle \log M(< r_n) \rangle = 2.5 \pm 0.6$. Figure 14 shows the distribution of sizes (r_{dec} and r_n) and integrated masses $[M(< r_{dec})$ and $M(< r_n)]$ for the modeled sample.

5.2. *Isothermal Mass*

In order to estimate the mass for those sources without models, and hence a best-fit p, the measured flux density was used to calculate a mass by assuming a single representative temperature. The isothermal total mass, M_{iso}, was calculated according to the equation

$$M_{iso} = \frac{S_\nu D^2}{B_\nu \kappa_\nu} = \left(5.09 \times 10^{-8}\ M_\odot\right) S_\nu(\mathrm{Jy}) D^2(\mathrm{pc}) (e^{41K/T_{iso}} - 1)\ , \quad (5)$$

which assumes a single dust temperature, T_{iso}. S_ν is the observed flux at 350 μm in a 120″ aperture and D is the distance. We assumed the OH5 opacity, $\kappa_\nu = 0.10$ cm^2 g^{-1} of gas and dust at 350 μm. Using the modeled sources with integrated masses, M_{int}, within a 120″ aperture, we can calculate what assumption about dust temperature would give the best agreement with the masses from the models. The "isothermal temperature," T_{iso}, is given by the equation

$$T_{iso} = \frac{h\nu/k}{\ln\{1 + [2h\nu^3 \kappa_\nu M_{int}(M_\odot)]/[c^2 S_\nu(\mathrm{Jy}) D^2(\mathrm{pc})]\}} \quad (6)$$

(Shirley et al. 2002b). For all the other cores, we assumed the mean temperature derived from the modeled sources, $\langle T_{iso} \rangle = 29 \pm 9$ K. This method allowed us to estimate the masses for the complete sample (see Table 4 and Fig. 8). We find $\langle M_{iso} \rangle = 2020 \pm 4410\ M_\odot$, a median $M_{iso} = 400\ M_\odot$, and $\langle \log M_{iso} \rangle = 2.8 \pm 0.7$. The distribution of M_{iso} is skewed to lower masses, but it has a tail of very massive cores.

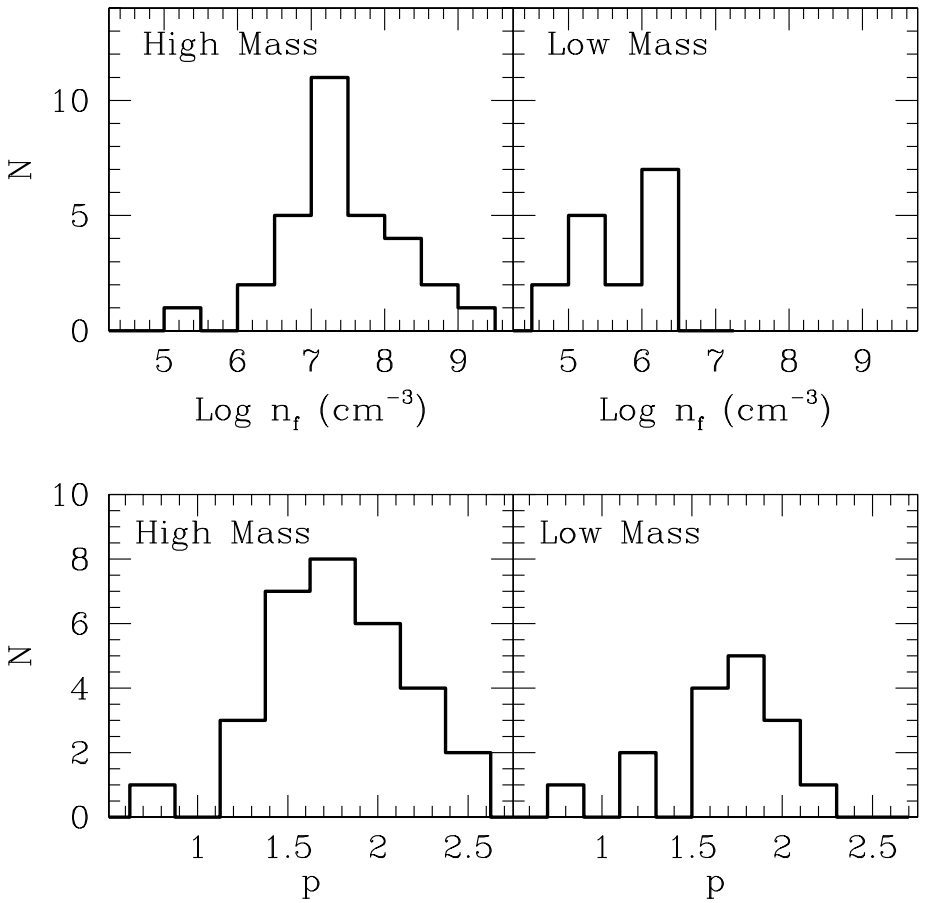

FIG. 13.—Histograms of fiducial densities (n_f) and best-fit density power-law exponents (p) for high- (*left*) and low-mass (*right*) star-forming cores modeled using the same methods. For the massive cores, $\langle n_f \rangle = 1.2 \times 10^8$ cm^{-3} and $\langle p \rangle = 1.8 \pm 0.4$. For the low-mass cores, $\langle n_f \rangle = 5.2 \times 10^5$ cm^{-3} and $\langle p \rangle = 1.6 \pm 0.4$; $\langle p \rangle = 1.8$ if sources with high aspect ratios are not included (Young et al. 2003).

5.3. *Mean Column Density*

The mean column density, Σ, has been used by McKee & Tan (2002; also Tan & McKee 2002) to derive fundamental physical quantities in regions forming massive stars. The observed Σ is a key parameter in the determination of the mean pressure, accretion rate, and star formation time (McKee & Tan 2002). Tan & McKee (2002) use the virial masses and radii from Plume et al. (1997) and report $\Sigma_{\rm vir} \approx 1$ g cm^{-2}. For comparison, we calculate Σ using the masses derived from the dust continuum for our subsample of Plume et al. (1997). For the modeled sample, using $M(< r_n)$ and r_n, $\Sigma_{\rm mod} = 0.19 \pm 0.12$ g cm^{-2}, which is significantly lower than $\Sigma_{\rm vir}$ (Tan & McKee 2002). However, expanding the calculation to the complete sample results in a more consistent value. Using the isothermal mass, $M_{\rm iso}$, and r_n (or $\langle r_n \rangle$ for the sources that were not modeled), $\Sigma = 0.73 \pm 1.7$ g cm^{-2}. The mass accretion rate, $\dot{m}_*$, varies as $\Sigma^{3/4}$ and the star formation time, t_{*f}, as $\Sigma^{-3/4}$; therefore, a lower Σ decreases the $\dot{m}_*$ and increases the t_{*f} given by McKee & Tan (2002).

It is important to note the inverse dependence of the masses and the mean column density on the opacity. Shirley et al. (2002a) compare the masses determined from the density distributions reported here with virial masses and find that the virial masses are larger on average by 3.4. While this is quite good agreement considering that the opacities from different dust models can vary up to a factor of 10 (Ossenkopf & Henning 1994), the masses and mean column density may be a factor of 3 larger.

6. DISCUSSION

6.1. *Comparison with Previous Models*

The average density distribution exponent, 1.8, is significantly higher than the 1.0–1.5 reported by van der Tak et al. (2000). Steeper best-fit power laws were also found for all of the sources in common. The van der Tak et al. (2000) best-fit models were based on molecular line emission observations and were not necessarily the best fits to their dust continuum emission (see their Fig. 8). However, there is still a discrepancy between their modeled 350 μm radial profiles and our models even though the same method was used. The difference stems from convolving the model with an observed beam rather than a 10″ Gaussian, as was done with the van der Tak et al. (2000) models. Figure 15 compares a modeled radial profile for GL 2591 using a 10″ Gaussian and the observed beam with $p = 2.0$ and all other parameters the same. The Gaussian beam requires a much shallower density power law to fit the observations. In the case of GL 2591, van der Tak et al. (2000) reported a best fit based on molecular line emission of $p = 1.0$ and show that the dust emission radial profile would be fitted by $p \sim 1.25$ (see their Fig. 8). We find $p = 2.0$; this was the largest discrepancy caused by the beam for the overlapping sample.

TABLE 4
MASSES AND SIZES

Source	r_{dec}[a] ($\times 10^4$ AU)	$M(< r_{dec})$[b] ($M_\odot$)	r_n[c] ($\times 10^4$ AU)	M_n[d] ($M_\odot$)	M_{iso}[e] ($M_\odot$)	L_{bol}/M_{iso} ($L_\odot/M_\odot$)
IRAS 00338+6312	1.0	10	12	810	50	24
G123.07−6.31	1.9	80	9.4	570	220	27
W3	1.6	...	...	...	180	140
W3(OH)	2.9	130	13	1210	1010	94
IRAS 02395+6244	4.6	...	...	...	210	260
IRAS 02461+6147	3.8	...	...	...	70	290
G137.07−3.00	1.9	...	...	...	80	...
GL 490	1.0	...	...	...	20	100
Ori-IRc2	0.5	...	...	...	240	410
S231	2.7	70	9.9	530	430	30
S235	2.7	...	...	...	100	100
S241	3.4	...	...	...	130	100
Mon R2	...	...	...	...	180	210
S252A	1.2	10	5.0	90	110	57
RCW 142	1.4	50	4.8	130	410	140
W28A2	1.4	200	9.0	790	1660	120
M8E	2.2	40	5.6	120	190	88
G9.62+0.10	4.8	670	12	1660	5780	61
G8.67−0.36	3.2	390	12	1470	3650	36
G10.60−0.40	4.6	1330	10	1960	12500	74
G12.42+0.50	1.8	50	5.4	140	300	64
G12.89+0.49	2.5	120	7.5	350	640	61
G12.21−0.10	5.3	...	...	...	6770	81
G13.87+0.28	5.3	190	7.7	300	1290	100
W33A	4.4	320	15	1990	2390	42
G14.33−0.64	1.9	150	9.8	800	880	20
GL 2136	1.7	20	5.2	90	320	200
G19.61−0.23	3.4	...	...	...	1290	140
G23.95+0.16	6.4	130	5.9	120	1690	110
G24.49−0.04	3.0	120	5.6	190	360	140
W43S	4.8	680	8.3	890	4940	320
G31.41+0.31	4.5	1500	15	3830	7150	33
G40.50+2.54	2.5	60	8.5	350	410	68
G35.58−0.03	3.4	...	...	...	230	190
G45.07+0.13	9.5	...	...	...	2620	460
G48.61+0.02	4.6	...	...	...	4350	230
W51M	5.0	...	...	...	28100	140
S87	2.2	...	...	...	260	190
S88B	4.4	50	4.6	50	260	270
ON 1	6.3	810	15	2390	3650	37
ON 2S	6.0	220	7.2	270	2410	150
S106	0.2	...	...	...	1030	490
GL 2591	0.8	10	2.9	20	68	290
G97.53+3.19	9.3	...	...	...	1030	...
BFS 11-B	...	...	...	...	60	130
S140	1.8	20	8.0	250	150	120
Cep A	1.0	10	11	280	120	180
S158	2.0	...	...	...	860	220
NGC 7538-1	3.7	150	11	750	1510	100
NGC 7538-9	3.1	60	5.6	120	400	180
S157	6.8	50	3.9	10	270	110

[a] The radius of the deconvolved FWHM size, θ_{dec}, of the 350 μm emission.
[b] The integrated mass within r_{dec}.
[c] The density equals 10^4 cm^{-3} at this radius.
[d] The integrated mass within r_n.
[e] Calculated with the isothermal temperature from eq. (6) for the modeled sample and $\langle T_{iso} \rangle = 29$ K for the sources that were not modeled.

On average, van der Tak et al. (2000) report a shallower power law by 0.4. If a 14″ Gaussian, which we find better describes the beam at the time of our observations, is used, the difference is also $\delta p = -0.75$ for GL 2591; the main effect is in the sidelobes.

6.2. *Comparison with Other Studies*

6.2.1. *Hatchell et al. (2000)*

Hatchell et al. (2000) modeled the 450 and 850 μm dust emission for five massive star-forming regions selected by

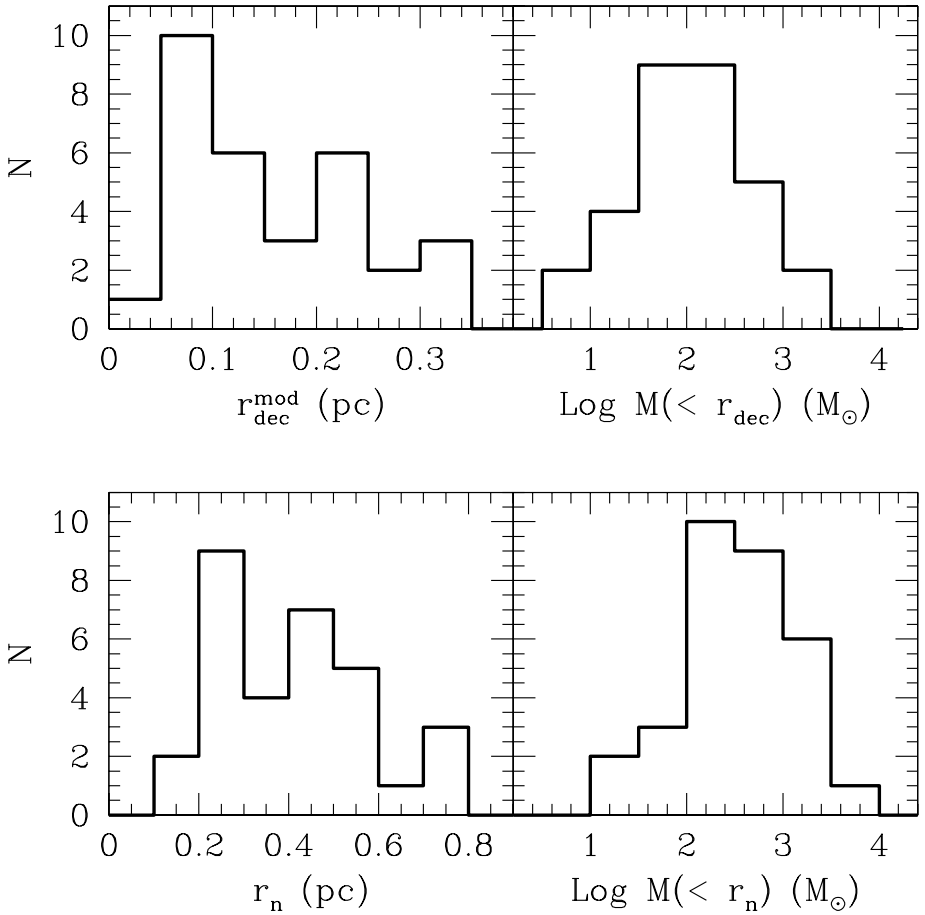

FIG. 14.—Distributions of radii and integrated masses for the modeled sample. *Top:* Histograms of r_{dec}^{mod} and the mass within r_{dec}. *Bottom:* Distributions of r_n, the radius at which the density falls to 10^4 cm^{-3}, and the mass within that radius.

emission from dense molecular gas. Three of their sources are included in this study (G12.21−0.10, G31.41+0.31, and G13.87+0.28). Hatchell et al. (2000) fit the SED and radial profile at 450 and 850 μm using the dust radiative transfer code DUSTY (Ivezić & Elitzur 1997). For G13.87+0.28, the only modeled source in common, Hatchell et al. (2000) report $p = 1.5$, which is shallower than our best fit $p = 1.75$. However, although $p = 1.0$ and 2.0 were ruled out by Hatchell et al. (2000), intermediate p-values were not investigated in their study.

Hatchell et al. (2000) find substantially higher masses (by a few times 10) than in our study. This discrepancy is due to the use of different dust properties. Hatchell et al. (2000) used Draine & Lee (1984) ice-free graphite and silicon dust grains as opposed to OH5 coagulated grains with ice mantles. The Draine & Lee (1984) opacities are much smaller and result in higher mass estimates.

Hatchell et al. (2000) included compact central cores in some of their models to fit the radial profiles. They found that the $p = 1.5$ density distribution was too shallow, but a central core with a $p = 1.5$ envelope fitted the data. Hatchell et al. (2000) used the core model for G12.21−0.10 and G31.41+0.31 because the 450 and 850 μm radial profiles fell off steeply within 20″. The 350 μm radial intensity profiles for these sources are also steeper than average. We report $p = 2.25$ for G31.41+0.31 although it was not well resolved with $\theta_{dec}/\theta_{mb} = 0.8$. G12.21−0.10 did not fit our modeling criteria because $\theta_{dec}/\theta_{mb} < 0.5$, so we considered it unresolved.

6.2.2. *Beuther et al.* (*2002*)

Beuther et al. (2002) studied the density structure of 69 regions forming massive stars (Sridharan at al. 2002) with 1.2 mm continuum and CS emission. Their resolution at 1.2 mm was very similar to ours at 350 μm, providing an interesting comparison. To determine the density structure, they fitted the radial intensity profiles with a broken power law, steeper in the outer region, and assumed a power-law temperature distribution ($T \propto r^{-0.4}$) to determine the density power law. We tested the effect of the power-law temperature distribution by modeling a source with $T \propto r^{-0.4}$ rather than the temperature distribution calculated from the dust code (see § 4). Assuming a power law resulted in less flux at shorter wavelengths, up to 60% at 25 μm, and a 20% higher n_f. However, the radial profile was unaffected and the best-fit p did not change. Therefore, the resultant density distributions from these studies can be reasonably compared.

Beuther et al. (2002) fitted the radial intensity profiles on average with $I \propto r^{-1.2}$ within 32″ and $r^{-1.8}$ in the outer regions. They report a mean density power-law index derived from the mean inner radial index of $\langle p \rangle = 1.6 \pm 0.5$. These results are consistent with our findings, although we have modeled the core envelopes well beyond 32″. As noted

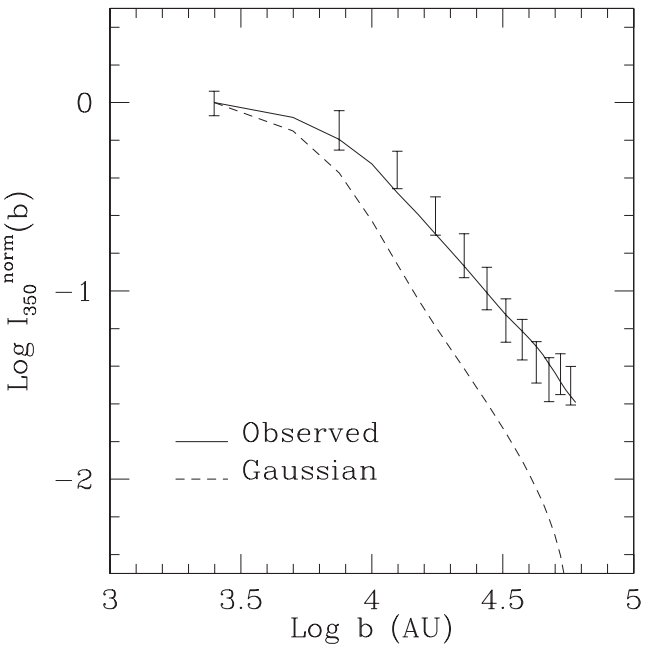

FIG. 15.—Model radial profile with $p = 2.0$ using the observed beam profile (*solid line*) and a 10″ Gaussian beam (*dotted line*) as used by van der Tak et al. (2000) plotted with the observed radial profile of GL 2591 (*error bars*). The error bars in the radial profiles represent the weighted mean variation in the annulus for which each point of the profile is calculated. The use of a 10″ Gaussian beam decreases the modeled p for GL 2591 by 0.75, accounting for the discrepancy in the value of p reported by van der Tak et al. (2000) (≈1.25) and in this study (2.0).

in § 3, we found no systematic tendency for intensity profiles to steepen beyond 40″. This difference between the two studies could reflect differences in the sample or differences in the observational details. For example, our chop throw was about twice that used by Beuther et al. (2002). More fundamentally, the agreement in the inner regions is very reassuring, indicating that observations from 350 to 1200 μm are tracing the same distribution in these sources.

Their sample has a mean mass, based on the integrated flux density and using either the unambiguous or near distance, of $\langle M \rangle = 1550\ M_\odot$. This should be compared to our $\langle M_{\rm iso} \rangle = 2020\ M_\odot$, which was derived in a similar way. However, they used different assumptions about opacities. Beuther et al. (2002) explain that the use of OH5 opacities, as used in our study, "would result in masses and column densities about a factor 4 lower." The factor of 4 makes their average masses about one-fifth of our mean value or about equal to the median $M_{\rm iso}$ (397 $M_\odot$). The Beuther et al. (2002) "OH5 scale" mass distribution is shifted to lower masses than the distribution of isothermal masses in this study (see Fig. 8) and peaks near $\log M = 2.2$ compared to $\log M_{\rm iso} = 2.8$. The discrepancy in the masses can further be explained by the use of different apertures in the measurement of flux densities between the two samples. Beuther et al. (2002) measure flux densities within the 5% level of the peak emission. In our study, the aperture was generally larger, 120″, resulting in larger flux densities. Since the isothermal mass is proportional to the flux density, we expect higher masses than Beuther et al. (2002).

Different methods were also used to calculate the luminosities. Sridharan et al. (2002) calculate the luminosities of the same sample studied by Beuther et al. (2002) by integrating a two-component graybody curve fit to *Infrared Astronomical Satellite* (*IRAS*) data. They find an average luminosity ($\langle L \rangle = 10^4\ L_\odot$) a factor of 25 lower than the mean luminosity reported here from integrating the observed SEDs, which in many cases also included *IRAS* fluxes. However, only a negligible fraction of this discrepancy is the result of different methods. For the two sources in common, Sridharan et al. (2002) find about a 20% lower luminosity than $L_{\rm obs}$ when the sources are placed at the same distances. Because of their selection against UCH II regions, the Sridharan et al. (2002) sample may contain younger and, therefore, less luminous sources than our sample. Sridharan et al. (2002) report a lower luminosity-to-mass ratio in their sample than that found in UCH II regions, implying that the ratio increases as a core evolves. In § 6.4 we discuss the luminosity-to-mass ratio of our sample.

6.3. *Comparison to Low-Mass Star Formation, Evolution, and Correlations*

Figure 13 shows a histogram of p-values for low-mass star-forming regions (Young et al. 2003; Shirley et al. 2002b) alongside the distribution of p for the massive stars in this study. Both samples were modeled with the techniques described here. For the low-mass cores, $\langle p \rangle = 1.6 \pm 0.4$ and increases to $\langle p \rangle = 1.8$ if cores with high aspect ratios are left out of the mean (Young et al. 2003). Although the modes of low- and high-mass star formation are drastically different, the distributions of p are strikingly similar. The mean fiducial density in the regions forming massive stars ($\langle n_f \rangle = 1.2 \times 10^8$ cm^{-3}) is over 2 orders of magnitude greater than that for the low-mass cores ($\langle n_f \rangle_{\rm low\text{-}mass} = 5 \times 10^5$ cm^{-3}; Fig. 13). Because the fiducial density is referred to 1000 AU, which we do not resolve, the absolute value should not be taken too literally; however, the similar values of p imply that the densities are higher at all radii by about 2 orders of magnitude in these sources than in cores forming low-mass stars. The similarity in p suggests that similar processes determine the *shape* of the density distribution in regions forming low- and high-mass stars.

In order to address the problem of a coherent evolutionary sequence for regions forming massive stars, we examine quantities commonly used as indicators of evolution in regions forming low-mass stars. One such indicator is the bolometric temperature, $T_{\rm bol}$ (Myers & Ladd 1993), the temperature of a blackbody with the same mean frequency as the observed SED. The range of bolometric temperatures in this study was relatively small, 46–173 K, compared to that found by Myers & Ladd (1993) for low-mass objects, almost 2 orders of magnitude. Another indicator is the ratio of total to submillimeter luminosity, $L_{\rm bol}/L_{\rm smm}$. For low-mass star-forming regions, both quantities are used as evolutionary indicators to mark the boundary between Class 0 and Class I sources; $L_{\rm bol}/L_{\rm smm}$ increases as a source evolves, and André et al. (1993) described sources with $L_{\rm bol}/L_{\rm smm} < 200$ as Class 0. Chen et al. (1995) defined Class 0 objects to be sources with $T_{\rm bol} < 70$ K. $T_{\rm bol}$ is plotted against $L_{\rm bol}/L_{\rm smm}$ in Figure 16, which shows that while the Class 0 and I definitions may not translate directly to massive stars, there is some correlation between the two measures. The trend implies that high bolometric temperature may be an indicator of more evolved sources. Young et al.

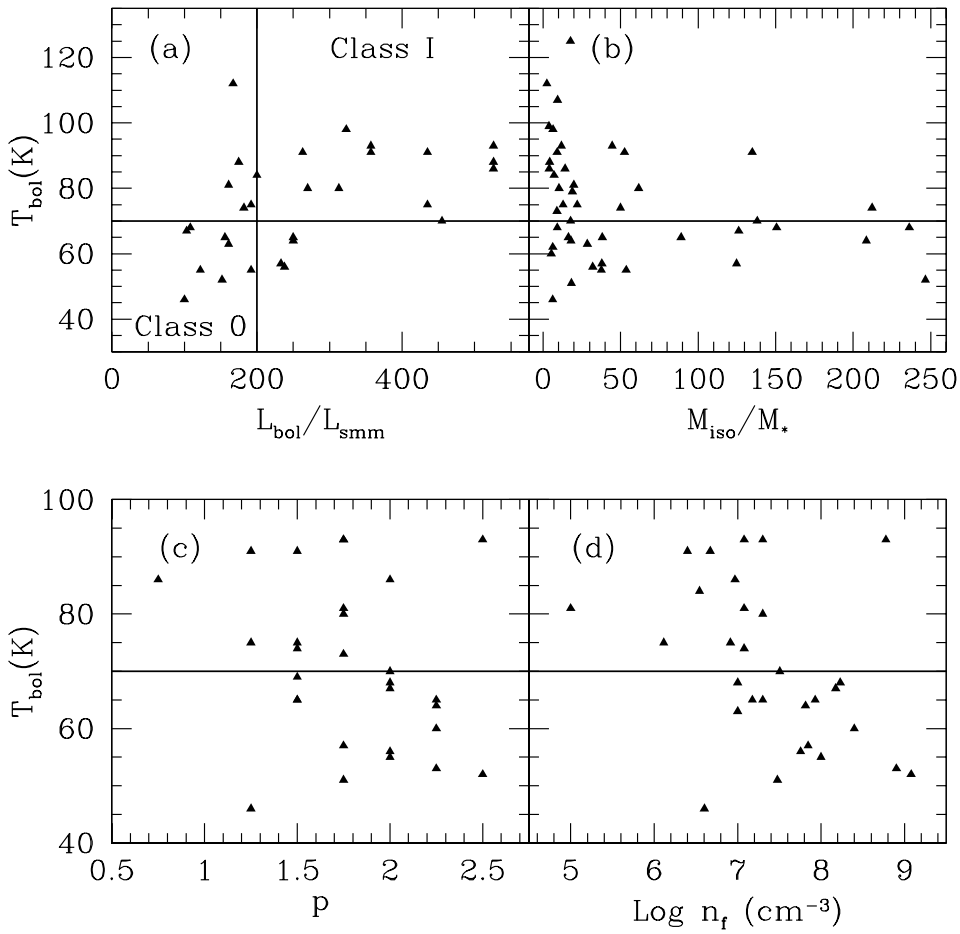

FIG. 16.—Relationships with T_{bol}. (*a*) Relationship between bolometric temperature and the ratio of total to submillimeter luminosity, both considered indicators of evolution in low-mass star-forming cores. The solid lines indicate the divisions between Class 0 and I low-mass protostars for each indicator. Class I sources have $T_{bol} > 70$ K and $L/L_{smm} > 200$. The linear correlation coefficient, r, is 0.52. (*b*) T_{bol} vs. another evolutionary indicator, M_{iso}/M_* where $M_* = L^{1/3.5}$ ($r = 0.06$). More evolved sources ($M_{iso}/M_* < 70$) have higher T_{bol} (>80). (*c*) T_{bol} vs. the density power-law index p ($r = -0.25$). (*d*) T_{bol} vs. the fiducial density, n_f, for the modeled sample ($r = -0.33$).

(2003) plot T_{bol} versus L_{bol}/L_{smm} for both low-mass sources and this sample and find that the Class 0/I boundary is not as clearly defined in regions forming low-mass stars as in high-mass regions.

Since T_{bol} may be an indicator of evolution, we looked for correlations with other parameters. Figure 16 shows no significant correlation between T_{bol} and p or n_f. Another indicator of evolution is the ratio of envelope to stellar mass (M_{iso}/M_*). As a source evolves and more material is accreted onto the central source, the ratio should decrease. To approximate the stellar mass, M_*, we assumed that the luminosity is dominated by a single massive star and that $M_* \propto L^{1/3.5}$. This mass-luminosity relationship is for zero-age main-sequence stars and has been used for a range of stellar masses (van der Tak et al. 2000; Shirley et al. 2002b). Observations of binary stellar masses and luminosities suggest that this relationship is valid to approximately 60 $M_\odot$ (Scalo 1986). The luminosities in this sample suggest that very few of these cores have a central source larger than 60 $M_\odot$, and the sources with the highest luminosities are likely forming more than one massive star. Figure 16 also shows that for regions forming massive stars there is not a significant correlation between T_{bol} and M_{iso}/M_*. However, the high values for T_{bol} (>80) occur for $M_{iso}/M_* < 70$, indicating a more evolved source.

Figure 17 plots M_{iso}/M_* and another potential evolutionary indicator, the FIR color (F_{60}/F_{100}), which is the ratio of flux densities at 60 and 100 μm, both observed with the same instrument (either *IRAS* or Kuiper Airborne Observatory; D. Jaffe 2001, private communication). Our data do not show the same direct correlation between FIR color and ratio of envelope to stellar mass as reported by van der Tak et al. (2000). However, their conclusion that bluer FIR colors only occur for lower mass ratios does apply. A more evolved source, as measured by an envelope-to-stellar mass ratio less than 70, may have a $T_{bol} > 100$ and FIR color, $F_{60}/F_{100} > 0.7$, while these values are never found for $M_{iso}/M_* > 70$. Figure 17 also plots p versus M_{iso}/M_* and indicates that less evolved sources (i.e., high M_{iso}/M_*) may have steeper than average density distributions.

Possible correlations with the density distribution were also examined; van der Tak et al. (2000) found no correlations between envelope mass or the internal luminosity and the density law exponent, p. However, Figure 18 shows that our larger sample does suggest some correlation with each of these parameters ($r \sim 0.5$). The density distribution steepens with increasing mass and luminosity. Figure 18 also plots the ratio of the deconvolved source diameter to the FWHM beam size, θ_{dec}/θ_{mb}, and the distance versus p. There is a strong relationship between θ_{dec}/θ_{mb} and the

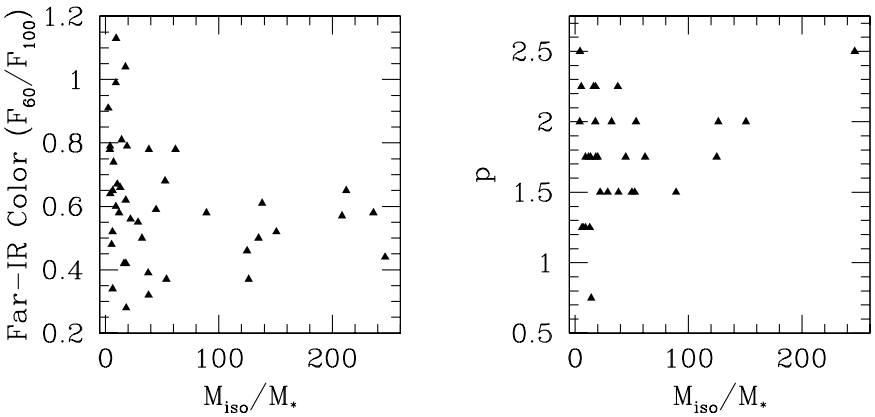

FIG. 17.—Relationships with the envelope-to-stellar mass ratio. *Left:* FIR color vs. M_{iso}/M_* ($r = 0.07$). More evolved sources ($M_{iso}/M_* < 70$) have bluer colors (>0.7). *Right:* p vs. M_{iso}/M_* ($r = 0.31$).

best-fit p. Better resolved sources tend to have shallower density profiles, as do more nearby sources. The correlation of θ_{dec}/θ_{mb} with p could be the result of a systematic effect in the models or resolution. Three of the six sources with $p > 2$ (G10.60−0.40, G31.41+0.31, and W43S) are also the most distant, suggesting that better resolution is needed to confirm their density distributions. The correlation of θ_{dec}/θ_{mb} with p could also indicate a physical difference in the cores, such as different initial conditions. Young et al. (2003) found the same correlation for low-mass cores where distance is not the same limiting factor as in this study. A source with a steeper density distribution (higher p)

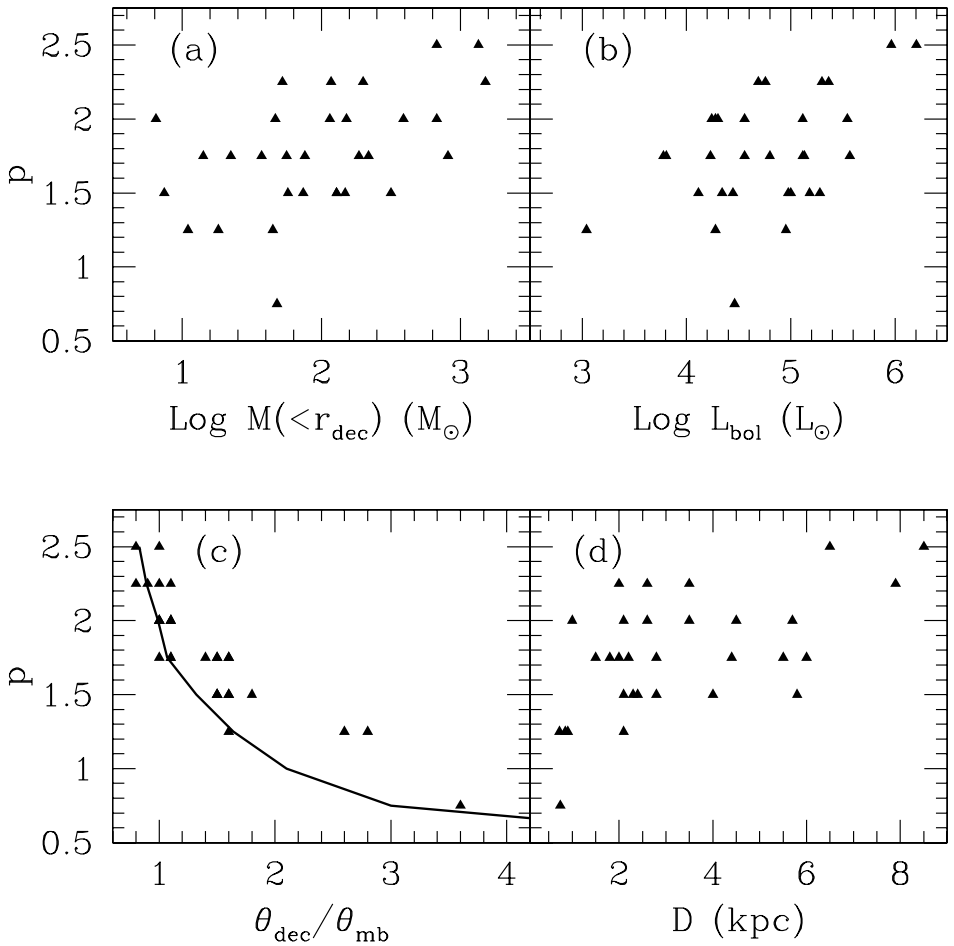

FIG. 18.—Relationships with p. (*a*) Density power-law index p vs. the logarithm of the mass within the 350 μm half-power radius ($r = 0.51$). (*b*) p vs. the logarithm of the modeled internal luminosity ($r = 0.49$). (*c*) p vs. the ratio of FWHM source size to beam size ($r = -0.86$). Only sources with $\theta_{dec}/\theta_{mb} \geq 0.8$ were modeled. Smaller sources have steeper density profiles. The solid line represents models of dust emission with $p = 0.5$–2.5. Sources significantly above the line (e.g., S140 and S88B) have extended aspherical emission. (*d*) p vs. distance ($r = 0.60$).

naturally has a smaller size (θ_{dec}) and will be less well resolved (Fig. 18*c*).

6.4. *Luminosity-to-Mass Ratios*

6.4.1. *Comparison to Galactic Studies*

The luminosity-to-mass ratio, L/M, is often used as a measure of the star formation rate per unit mass. Most studies in our Galaxy have used the mass of the entire molecular cloud, determined from CO emission. The resulting average ($L/M = 0.4\ L_\odot/M_\odot$) is quite low (Bronfman et al. 2000). For molecular clouds that contain H II regions, the luminosity-to-mass ratio from CO emission is an order of magnitude higher, $L/M = 4\ L_\odot/M_\odot$ (Mooney & Solomon 1988), but the dispersion is over 2–3 orders of magnitude (Evans 1991; Mead, Kutner, & Evans 1990). CO emission traces the less dense gas of the entire molecular cloud, while the dust continuum emission at submillimeter wavelengths measures the mass of very dense gas actually involved in star formation. We computed values of L_{bol}/M_{iso} because M_{iso} could be obtained for the largest number of sources. Figure 19 plots $\log(L_{bol}/M_{iso})$ versus $\log M_{iso}$. Both L_{bol} and M_{iso} are proportional to the square of the distance, so the distance uncertainties are minimized in the ratio. The ratio and, hence, the star formation rate per unit mass are constant over the entire mass range. The dispersion of $\log(L_{bol}/M_{iso})$ is about 1.5 orders of magnitude, which is significantly less than the 2–3 orders of magnitude when the mass is traced by CO.

Figure 19 also plots $\log L_{bol}$ versus $\log M_{iso}$ and shows that the luminosity-to-mass ratio traced in massive cores is significantly higher than the average L/M in molecular clouds with H II regions. Figure 20 shows the distribution of $\log(L_{bol}/M_{iso})$, which peaks near $\langle\log(L_{bol}/M_{iso})\rangle = 2.0 \pm 0.4$; the median $\log(L_{bol}/M_{iso})$ is also 2.0. The mean value of the ratio is $\langle L_{bol}/M_{iso}\rangle = 140 \pm 100\ L_\odot/M_\odot$, with a median value of 120 $L_\odot/M_\odot$. This $\langle L_{bol}/M_{iso}\rangle$ is 30 times that derived from CO for Galactic molecular clouds containing H II regions. Clearly the star formation rate per unit mass of *dense* gas is much higher, indicating that the dense gas traced by submillimeter emission is the location of massive star formation.

The histogram of L_{bol}/M_{iso} in Figure 20 shows that the distribution is strongly skewed. Most sources have low ratios, but there is a tail of very high ratios, reaching up to 490 $L_\odot/M_\odot$. A few sources could be affected by confusion with multiple sources in the large *IRAS* beam, resulting in a luminosity that is too high. This problem is difficult to avoid since *IRAS* is often the only source of mid- to far-IR fluxes. Higher spatial resolution is needed to eliminate multiple source confusion in flux measurements. The Stratospheric Observatory for Infrared Astronomy (SOFIA) that will fly later in the decade will be ideally suited to address this problem and fix the upper limit to L/M for Galactic sources.

The mean L/M for the Beuther et al. (2002) sample ($\langle L/M\rangle = 20 \pm 18\ L_\odot/M_\odot$; Sridharan et al. 2002) is 7 times lower than in this study ($\langle L_{bol}/M_{iso}\rangle = 140\ L_\odot/M_\odot$). If we decrease their masses by a factor of 4, putting them on the "OH5 scale," the values are in better agreement ($\langle L/M\rangle \sim 80\ L_\odot/M_\odot$). For sources with a distance ambiguity, we assume their near distance, which may produce a downward bias in luminosities and masses. Eliminating this bias by averaging only sources in their sample for which the distance is not ambiguous gives a luminosity-to-mass ratio ($\langle L/M\rangle = 120 \pm 90\ L_\odot/M_\odot$) that is consistent with the results of our study. However, Sridharan et al. (2002) report an L/M significantly smaller than that of a sample of UCH II regions (Hunter 1997; Hunter et al. 2000). They suggest that the cores in their sample are in a younger pre–UCH II phase and that L/M increases as the cores evolve and develop UCH II regions (Sridharan et al. 2002). Hunter et al. (2000) describe their sample as having UCH II region FIR colors or thermal radio continuum emission. If we also convert the opacities used by Hunter et al. (2000) to the OH5 scale, then the average luminosity-to-mass ratio for their sample is $\langle L/M\rangle = 280 \pm 370\ L_\odot/M_\odot$ with a median of 150. The mean L/M for the UCH II regions studied by Hunter (1997) and Hunter et al. (2000) is higher, but the median is not inconsistent with the results of the work presented here for cores both with and without UCH II regions.

In order to test the hypothesis that the luminosity-to-mass ratio increases as a massive star-forming region develops a UCH II region, we divided our sample and calculated L_{bol}/M_{iso} for cores with and without UCH II regions. We do

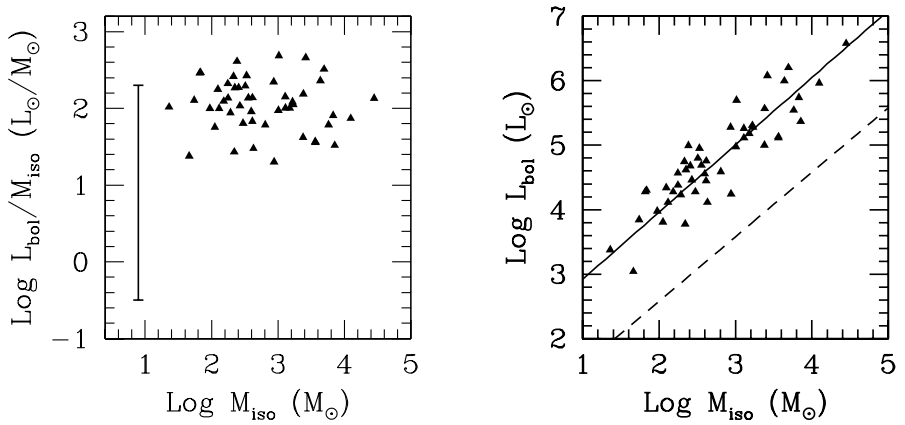

FIG. 19.—*Left:* Plot of $\log(L_{bol}/M_{iso})$ vs. $\log M_{iso}$. The dispersion in $\log(L_{bol}/M_{iso})$ is about 1.5 orders of magnitude, significantly less than in CO observations (2–3 mag). The error bar shows the full range from the CO observations (Evans 1991). *Right:* Plot of the logarithm of L_{bol} vs. the logarithm of M_{iso} ($r = 0.89$). The solid line is the least-squares fit to the data $\log L_{bol} = 1.9 + \log M_{iso}$. The dashed line is based on CO masses for molecular clouds containing H II regions, $\log L_{bol} = 0.58 + \log M_{iso}$ (Mooney & Solomon 1988). The luminosity-to-mass ratio is much higher in massive star-forming cores than in molecular clouds.

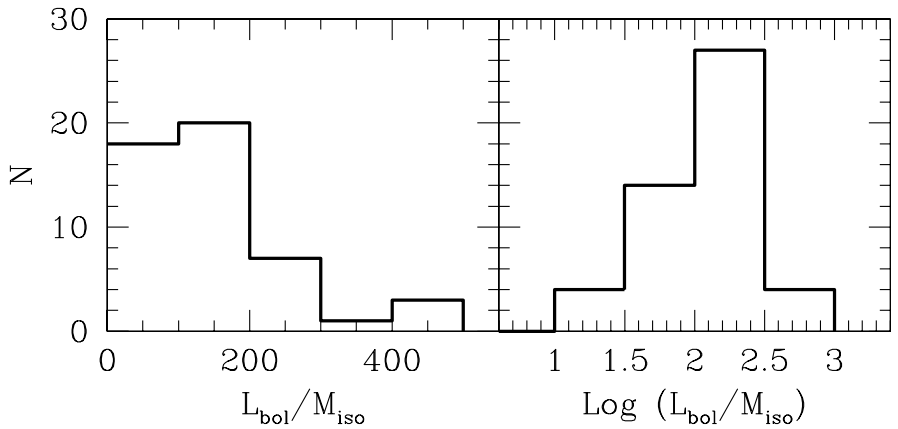

FIG. 20.—Distribution of the luminosity-to-mass ratio, L_{bol}/M_{iso} (*left*), and $\log(L_{bol}/M_{iso})$ (*right*). The histogram of L_{bol}/M_{iso} shows a tail of high ratios out to 490 $L_\odot/M_\odot$.

not find the same disparity in L/M between our two subsamples as between the results of Sridharan et al. (2002) and those of Hunter (1997) and Hunter et al. (2000). For the cores associated with UCH II regions, $\langle L_{bol}/M_{iso}\rangle = 170 \pm 130$ (with a median of 120), which is lower than the mean of the sample of Hunter (1997) and Hunter et al. (2000), but within the dispersions of the two samples. The mean ratio of the remaining cores that do not contain a UCH II region is not significantly lower, $\langle L_{bol}/M_{iso}\rangle = 130 \pm 90$ with a median of 100. However, in a CS study with a larger sample of which ours is a subset, Shirley et al. (2002a) found that the median luminosity–to–virial mass ratio is more than a factor of 2 higher in cores with UCH II regions than in cores without UCH II regions.

6.4.2. *Comparison with Extragalactic Studies*

Submillimeter wavelengths are becoming increasingly important in the study of star formation in other galaxies, especially at high redshifts (Blain et al. 2002). A recent submillimeter survey measured the dust masses, M_D, and FIR to submillimeter ($\sim$1–1000 μm) luminosities, L_{FIR}, of bright local *IRAS* galaxies (Dunne & Eales 2001). Dust is often used as a tracer of mass for more distant sources as well (e.g., Omont et al. 2002; Calzetti et al. 2000; Benford et al. 1999). These studies assume a single dust temperature, usually 50 K, based on the FIR and submillimeter SEDs of the galaxies (e.g., Calzetti et al. 2000; Benford et al. 1999). The average T_{iso} of 29 K found in this study is substantially lower. If we compared the mass within r_{dec}, we found that T_{iso} was about 50 K, but when using the full extent, much cooler dust contributed substantially. The dust mass, M_D, of galaxies is usually calculated in the same way as our M_{iso} (eq. [5]). However, different opacities are used and only the mass of the dust is calculated, not the mass of gas and dust as with M_{iso}.

For high-redshift ($z > 4$) quasars, Omont et al. (2002) report a mean (and median) dust mass, $\langle M_D\rangle \sim 5 \times 10^8\ M_\odot$ for a range of 2×10^8–$1 \times 10^9\ M_\odot$. A typical FIR luminosity (>50 μm) for their sample is $L_{FIR} \sim 10^{13}\ L_\odot$, giving $L_{FIR}/M_D = 2 \times 10^4\ L_\odot/M_\odot$. For purposes of comparison, we calculated an isothermal dust mass, M_D, using the same temperature (50 K) and opacities as Omont et al. (2002). For the regions in this study, $\langle L_{obs}/M_D\rangle = (1.4 \pm 1.0) \times 10^4\ L_\odot/M_\odot$ ranging from 2×10^3 to 4.5×10^4 $L_\odot/M_\odot$. The luminosity-to-mass ratio for high-redshift quasars is similar to the higher values in our sample, suggesting that starbursts form stars as if most of their molecular material acts like the most extreme regions forming massive stars in the Milky Way. However, starbursts might not be the only source of L_{FIR} in distant quasars. Omont et al. (2002) suggest central active galactic nuclei as another source of dust heating. In that case, the star-forming L/M would be smaller.

7. SUMMARY

We have presented dust continuum maps of 51 regions forming massive stars with a large range of sizes and masses, $\langle r_{dec}\rangle = 0.16 \pm 0.10$ pc and $\langle M_{iso}\rangle = 2020 \pm 4410\ M_\odot$. We find that the peak of the dust emission is more often coincident with the water maser position than the UCH II region, implying that the dust may better trace the earlier stages of massive star formation. Modeling a subset of 31 sources yielded a mean density index for power laws $[n(r) = (r/r_f)^{-p}]$ of $\langle p\rangle = 1.8 \pm 0.4$. The dispersion is about twice the expected uncertainty for an individual source, suggesting some real dispersion among sources. The mean value for p is incompatible with a logatropic sphere ($p = 1$), but $p = 1.5$ and 2 are possible. The mean value and variation in p are similar to those found for low-mass regions (Young et al. 2003).

For the modeled sources, integrated masses within two different fiducial radii were presented in addition to the isothermal masses. The mean mass within the 350 μm half-power radius (r_{dec}) is $\langle M(< r_{dec})\rangle = 250 \pm 380\ M_\odot$. For the larger, more physical radius where the density falls off to the ambient level ($n = 10^4$ cm^{-3}), $\langle M(< r_n)\rangle = 720 \pm 860\ M_\odot$. The mean column density for the complete sample was found to be $\Sigma = 0.73 \pm 1.7$ g cm^{-2}. However, because of the inverse dependency of mass on opacity, comparison with virial masses suggests that the masses and mean surface density could be about a factor of 3 larger.

The density structure of massive star-forming cores was found to be consistent with Beuther et al. (2002). The results were also consistent with van der Tak et al. (2000) when the difference in a Gaussian and the observed beam profile was taken into account. Our data also confirm some of the conclusions made by van der Tak et al. (2000) with respect to

possible evolutionary indicators. There is a trend of rising $T_{\rm bol}$ with increasing $L/L_{\rm smm}$, suggesting that either of these quantities could be tracing evolution.

The luminosity-to-mass ratio, a tracer of star formation rate per unit mass, has a mean of $\langle L_{\rm bol}/M_{\rm iso}\rangle = 140 \pm 100$ $L_\odot/M_\odot$ for dense gas traced by dust emission, with a tail extending up to about 500 $L_\odot/M_\odot$. These values are much higher than those based on masses from CO emission. The mean luminosity-to-mass ratio derived using the dust mass is similar to that in extreme starburst galaxies, especially those seen at substantial redshift.

We thank the staff of the Caltech Submillimeter Observatory for assistance in using SHARC. We are very grateful to R. Chamberlain for providing sky opacity information from the CSO tippers. We also thank T. Hunter, D. Benford, R. Chamberlin, and D. Lis for technical assistance, sometimes via phone calls at inconvenient times. We are grateful to R. Forster and D. Jaffe for their generous sharing of data and useful comments. We thank NSF (grant AST 99-88230) and the state of Texas for support.

REFERENCES

André, P., Ward-Thompson, D., & Barsony, M. 1993, ApJ, 406, 122
Benford, D. J., Cox, P., Omont, A., Phillips, T. G., & McMahon, R. G. 1999, ApJ, 518, L65
Beuther, H., Schilke, P., Menten, K. M., Motte, F., Sridharan, T. K., & Wyrowski, R. 2002, ApJ, 566, 945
Blain, A. W., Smail, I., Ivison, R. J., Kneib, J.-P., & Frayer, D. T. 2002, Phys. Rep., in press
Blitz, L., Fich, M., & Stark, A. A. 1982, ApJS, 49, 183
Bronfman, L., Casassus, S., May, J., & Nyman, L.-A. 2000, A&A, 358, 521
Bronfman, L., Nyman, L.-A., & May, J. 1996, A&AS, 115, 81
Calzetti, D., Armus, L., Bohlin, R. C., Kinney, A. L., Koornneef, J., & Storchi-Bergmann, T. 2000, ApJ, 533, 682
Carpenter, J. M. 2000, AJ, 120, 3139
Cesaroni, R., Palagi, F., Felli, M., Catarzi, M., Comoretto, G., Di Franco, S., Giovanardi, G., & Palla, F. 1988, A&AS, 76, 445
Chen, H., Myers, P. C., Ladd, E. F., & Wood, D. O. S. 1995, ApJ, 445, 377
Cheung, L. H., Frogel, J. A., Gezari, D. Y., & Hanser, M. G. 1980, ApJ, 240, 74
Chini, R., Henning, Th., & Pfau, W. 1991, A&A, 247, 157
Chini, R., Kreysa, E., Mezger, P. G., & Gemuend, H.-P. 1986a, A&A, 154, L8
———. 1986b, A&A, 157, L1
Chini, R., Kruegel, E., & Kreysa, E. 1986c, A&A, 167, 315
Churchwell, E., Wolfire, M. G., & Wood, D. O. S. 1990, ApJ, 354, 247
De Buizer, J. M. 2000, Ph.D. thesis, Univ. Florida
Dent, W. R. F., MacDonald, G. H., & Anderson, M. 1988, MNRAS, 235, 1397
Dent, W. R. F., Matthews, H. E., & Ward-Thompson, D. 1998, MNRAS, 301, 1049
Draine, B. T., & Lee, H. M. 1984, ApJ, 285, 89
Dunne, L., & Eales, S. A. 2001, MNRAS, 327, 697
Dyck, H. M., & Simon, T. 1977, ApJ, 211, 421
Egan, M. P., Leung, C. M., & Spagna, G. R. 1988, Comput. Phys. Commun., 48, 857
Elitzur, M., Hollenbach, D. J., & McKee, C. F. 1989, ApJ, 346, 983
Ellis, H. B., Jr., Lester, D. F., Harvey, P. M., Joy, M., Telesco, C. M., Decher, R., & Werner, M. W. 1990, ApJ, 365, 287
Emerson, D. T., Klein, U., & Haslam, C. G. T. 1979, A&A, 76, 92
Evans II, N. J., 1991, in ASP Conf. Ser. 20, Frontiers of Stellar Evolution, ed. D. L. Lambert (San Francisco: ASP), 45
———. 1999, ARA&A, 37, 311
Evans II, N. J., Beckwith, S., Brown, R. L., & Gilmore, W. 1979, ApJ, 227, 450
Evans II, N. J., Beichman, C., Gatley, I., Harvey, P., Nadeau, D., & Sellgren, K. 1981a, ApJ, 246, 409
Evans II, N. J., Rawlings, J. M. C., Shirley, Y. L., & Mundy, L. G. 2001, ApJ, 557, 193
Evans II, N. J., Shirley, Y. L., Mueller, K. E., & Knez, C. 2002, in ASP Conf. Ser. 267, Hot Star Workshop III: The Earliest Phases of Massive Star Birth, ed. P. A. Crowther (San Francisco: ASP), 17
Evans II, N. J., et al. 1981b, ApJ, 244, 115
Fazio, G. G., Lada, C. J., Kleinmann, D. E., Wright, E. L., Ho, P. T. P., & Low, F. J. 1978, ApJ, 221, L77
Garay, G., & Lizano, S. 1999, PASP, 111, 1049
Gezari, D. Y., Backman, D. E., & Werner, M. W. 1998, ApJ, 509, 283
Gordon, M. A. 1990, ApJ, 352, 636
Guertler, J., Henning, Th., Kruegel, E., & Chini, R. 1991, A&A, 252, 801
Hatchell, J., Fuller, G. A., Millar, T. J., Thompson, M. A., & MacDonald, G. H. 2000, A&A, 357, 637
Hoare, M. G., Roche, P. F., & Glencross, W. M. 1991, MNRAS, 251, 584
Hofner, P., Kurtz, S., Churchwell, E., Walmsley, C. M., & Cesaroni, R. 1996, ApJ, 460, 359
Hunter, T. R. 1997, Ph.D. thesis, Caltech
Hunter, T. R., Benford, D. J., & Serabyn, E. 1996, PASP, 108, 1042
Hunter, T. R., Churchwell, E., Watson, C., Cox, P., Benford, D. J., & Roelfsema, P. R. 2000, AJ, 119, 2711
IRAS PSC 1988, ed. C. Beichman et al. (NASA RP-1190; Washington: GPO)
Ivezić, Z., & Elitzur, M. 1997, MNRAS, 287, 799
Jaffe, D. T., Hildebrand, R. H., Keene, J., Harper, D. A., Loewenstein, R. F., & Moran, J. M. 1984, ApJ, 281, 225
Jenness, T. 1996, Ph.D. thesis, Cambridge Univ.
Jenness, T., Scott, P. F., & Padman, R. 1995, MNRAS, 276, 1024
Kastner, J. H., Weintraub, D. A., Snell, R. L., Sandell, G., Aspin, C., Hughes, D. H., & Bass, F. 1994, ApJ, 425, 695
Kennicutt, R. C., Jr. 1998, ARA&A, 36, 189
Koppenaal, K., van Duinen, R. J., Aalders, J. W. G., Sargent, A. I., & Nordh, L. 1979, A&A, 75, L1
Kurtz, S., Churchwell, E., & Wood, D. O. S. 1994, ApJS, 91, 659
Lada, C. J. 1987, in IAU Symp. 115, Star Formation Regions, ed. M. Peimbert & J. Jugaku (Dordrecht: Reidel), 1
Lada, C. J., Thronson, H. A., Jr., Smith, H. A., Schwartz, P. R., & Glaccum, W. 1984, ApJ, 286, 302
Lada, C. J., & Wilking, B. A. 1984, ApJ, 287, 610
Lebofsky, M. J., Kleinmann, S. G., Reike, G. H., & Low, F. J. 1976, ApJ, 206, L157
McCutcheon, W. H., Sato, T., Purton, C. R., Matthews, H. E., & Dewdney, P. E. 1995, AJ, 110, 1762
McKee, C. F., & Tan, J. C. 2002, Nature, 416, 59
McLaughlin, D. E., & Pudritz, R. E. 1997, ApJ, 476, 750
Mead, K. N., Kutner, M. L., & Evans II, N. J. 1990, ApJ, 354, 492
Mitchell, G. F., Hasegawa, T. I., & Schella, J. 1992, ApJ, 386, 604
Mookerjea, B., Ghosh, S. K., Karnik, A. D., Rengarajan, T. N., Tandon, S. N., & Verna, R. P. 1999, ApJ, 522, 285
Mookerjea, B., Ghosh, S. K., Rengarajan, T. N., Tandon, S. N., & Verna, R. P. 2000, AJ, 120, 1954
Mooney, T. J., Shivers, A., Mezger, P. G., Solomon, P. M., Krey, S. E., Haslam, C. G. T., & Lemke, R. 1995, A&A, 299, 869
Mooney, T. J., & Solomon, P. M. 1988, ApJ, 334, L51
Moriarty-Schieven, G. H., Snell, R. L., & Hughes, V. A. 1991, ApJ, 374, 169
Myers, P. C., & Ladd, E. F. 1993, ApJ, 413, L47
Olmi, L., & Cesaroni, R. 1999, A&A, 352, 266
Omont, A., Cox, P., Bertoldi, F., McMahon, R. G., Carilli, C., & Isaak, K. G. 2002, A&A, in press
Osorio, M., Lizano, S., & D'Alessio, P. 1999, ApJ, 525, 808
Ossenkopf, V., & Henning, Th. 1994, A&A, 291, 943
Palagi, F., Cesaroni, R., Comoretto, G., Felli, M., & Natale, V. 1993, A&AS, 101, 153
Pipher, J. L., et al. 1977, A&A, 59, 215
Plume, R., Jaffe, D. T., & Evans II, N. J. 1992, ApJS, 78, 505
Plume, R., Jaffe, D. T., Evans II, N. J. Martin-Pintado, J., & Gomez-Gonzalez, J. 1997, ApJ, 476, 730
Richardson, K. J., White, G. J., Sandell, G., Duncan, W. D., & Krisciunas, K. 1989, A&A, 221, 95
Sandell, G. 1994, MNRAS, 271, 75
Sandell, G., & Weintraub, D. A. 2001, ApJS, 134, 115
Scalo, J. M. 1986, Fundam. Cosmic Phys., 11, 1
Schloerb, F. P., Snell, R. L., & Schwartz, P. R. 1987, ApJ, 319, 426
Schwartz, P. R., & Spencer, J. H. 1977, MNRAS, 180, 297
Scott, P. F. 1978, MNRAS, 183, 435
Shirley, Y. L., Evans II, N. J. Mueller, K. E., Knez, C., & Jaffe, D. T. 2002a, ApJS, submitted
Shirley, Y. L., Evans II, N. J. & Rawlings, J. M. C. 2002b, ApJ, 575, 337
Shirley, Y. L., Evans II, N. J. Rawlings, J. M. C., & Gregerson, E. M. 2000, ApJS, 131, 249
Shu, F. H. 1977, ApJ, 214, 488
Simon, M., Peterson, D. M., Longmore, A. J., Storey, J. M. V., & Tokumaga, A. T. 1985, ApJ, 298, 328
Soifer, B. T., & Pipher, J. L. 1975, ApJ, 199, 663
Sridharan, T. K., Beuther, H., Schilke, P., Menten, K. M., & Wyrowski, F. 2002, ApJ, 566, 931
Stier, M. T. 1984, ApJ, 283, 573
Tan, J. C., & McKee, C. F. 2002, in ASP Conf. Ser. 267, Hot Star Workshop III: The Earliest Phases of Massive Star Birth, ed. P. A. Crowther (San Francisco: ASP), 267

Thompson, R. 1984, ApJ, 283, 165
Thronson, H. A., Jr., Gatley, I., Harvey, P. M., Sellgren, K., & Werner, M. W. 1980, ApJ, 237, 66
Thronson, H. A., Jr., Lowenstein, R. F., & Stokes, G. M. 1979, AJ, 84, 1328
Tofani, G., Felli, M., Talor, G. B., & Hunter, T. R. 1995, A&AS, 112, 299
Tothill, N. F. H. 1999, Ph.D. thesis, London Univ.
Val'tts, I. E., Ellingsen, S. P., Slysh, V. I., Kalenskii, S. V., Otrupcek, R., & Larionov, G. M. 2000, MNRAS, 317, 315
van der Tak, F. F. S., van Dishoeck, E. F., Evans II, N. J. Bakker, E. J., & Blake, G. A. 1999, ApJ, 522, 991
van der Tak, F. F. S., van Dishoeck, E. F., Evans II, N. J. & Blake, G. A. 2000, ApJ, 537, 283
Walker, C. K., Adams, F. C., & Lada, C. J. 1990, ApJ, 349, 515
Walsh, A. J., Bertoldi, F., Burton, M. G., & Nikola, T. 2001, MNRAS, 326, 36
Walsh, A. J., Burton, M. G., Hyland, A. R., & Robinson, G. 1998, MNRAS, 301, 640
Werner, M. W., Becklin, E. E., Gatley, I., Matthews, K., Neugebauer, G., & Wynn-Williams, C. G. 1979, MNRAS, 188, 463
Wilner, D. J., Welch, W. J., & Forster, J. R. 1995, ApJ, 449, L73
Wood, D. O. S., & Churchwell, E. 1989, ApJ, 340, 265
Wright, E. L., Lada, C. J., Fazio, G. G., Low, F. J., & Kleinman, D. E. 1977, AJ, 82, 132
Yang, J., Umemoto, T., Iwata, T., & Fukui, Y. 1991, ApJ, 373, 137
Young, C. H., Shirley, Y. L., Evans II, N. J. & Rawlings, J. M. C. 2003, ApJS, in press
Zhou, S., Butner, H. M., Evans II, N. J. Guesten, R., Kutner, M. L., & Mundy, L. G. 1994, ApJ, 428, 219
Zhou, S., Evans II, N. J. & Wang, Y. 1996, ApJ, 466, 296
Zinchenko, I., Forsstroem, V., Lapinov, A., & Mattila, K. 1994, A&A, 288, 601